

NASA Contractor Report 3669

NASA
CR
3498-
pt.2
c.1

Numerical Studies of Laminar and Turbulent Drag Reduction - Part II

TECH LIBRARY KAFB, NM
0062248

AFWL/SUL
TECHNICAL LIBRARY
KIRTLAND AFB, NM 87117

R. Balasubramanian and S. A. Orszag

CONTRACT NAS1-16722
JANUARY 1983

NASA



NASA Contractor Report 3669

Numerical Studies of Laminar and Turbulent Drag Reduction - Part II

R. Balasubramanian and S. A. Orszag
Cambridge Hydrodynamics, Inc.
Cambridge, Massachusetts

Prepared for
Langley Research Center
under Contract NAS1-16722



National Aeronautics
and Space Administration

**Scientific and Technical
Information Branch**

1983

List of Contents

Summary	v
Introduction	1
Laminar Flow Over Wavy Surfaces	3
Influence of Surface Waviness on Flow Stability	16
Methodology for Evaluating the Drag Reduction Characteristics of Wavy Surfaces	22
Nonplanar Surfaces for Drag Reduction in Laminar Boundary Layers	27
The Effect of Suction/Injection on the Total Drag of a Wavy Surfaces	29
Drag Characteristics of Nonplanar Waveforms in Turbulent Flow	32
Secondary Instability of Wall Bounded Shear Flows	52
Secondary Instabilities of Free Shear Flows	56
Black Box Version of Compressible Sally Code	56
References	58

List of Tables

Table

- 1.1 Comparison of Navier Stokes solutions and Benjamin's theory;
 $R_x = 100$; $x/\lambda = 10$; $\delta/\lambda = 5.0$.
- 1.2 Comparison of Navier Stokes solutions and Benjamin's theory;
 $R_x = 1000$; $x/\lambda = 10$; $\delta/\lambda = 1.58$.
- 1.3 Comparison of Navier Stokes solutions and Benjamin's theory;
 $R_x = 10^4$; $x/\lambda = 10$; $\delta/\lambda = 0.5$.
- 1.4 Effect of δ/λ on C_p . Comparison between Navier Stokes solutions and Benjamin theory; $R_x = 10^4$; $a/\lambda = 10^{-3}$.
- 1.5 Test on validity of Couette flow analysis;
 $R_\lambda = 10^4$; $X/\lambda = 1, 2, 4$.

List of Figures

Figure

- 3.1 Plot of pressure at a point on a wavy surface vs time.
 $Re_x = 10^4$, $a/\lambda = 10^{-3}$, $\lambda/x = 0.012$
- 3.2 Plot of pressure at a point over a wavy surface vs time.
 $Re_x = 10^4$, $a/\lambda = 10^{-3}$, $\lambda/X = 0.060$
- 3.3 Plot of pressure at a point over a wavy surface vs time.
 $Re_x = 10^5$, $a/2 = 2.5 \times 10^{-4}$; $X/\lambda = 5$; $\alpha = 0.1709$
- 3.4 Plot of pressure at a point 1 on a wavy surface
 $R_x = 10^5$ $a/\lambda = 10^{-3}$; $X/\lambda = 10$; $\alpha = 0.34175$
- 3.5 Plot of pressure at point 2 (separated by $\lambda/8$ from point 1) vs time.
 Note that the pressure signal is shifted by a constant time unit from that in Fig (3.4).
- 3.6 Plot of pressure vs time for a wavy surface.
 $R_x = 10^5$; $a/\lambda = 5 \times 10^{-3}$; $\alpha = 0.34175$; $x/\lambda = 10$
- 3.7 Plot of pressure vs time at a point for a wavy surface.
 $R_x = 10^5$; $a/\lambda = 10^{-2}$; $\alpha = 0.34175$; $x/\lambda = 10$
- 3.8 Plot of pressure vs time at a point for a wavy surface.
 $R_x = 10^5$; $a/\lambda = 3 \times 10^{-2}$; $\alpha = 0.34175$; $x/\lambda = 10$
 Flow separation occurs for this case.
- 3.9 Plot of pressure vs time at a point on a wavy surface.
 $R_x = 10^5$; $a/\lambda = 5 \times 10^{-2}$; $\alpha = 0.34175$; $x/\lambda = 10$
 Flow separation over the wave. Breakdown of calculations occurs in convective time scale.
- 3.10 Plot of pressure at a point over a wave.
 $R_x = 5 \times 10^5$; $a/\lambda = 10^{-3}$; $x/\lambda = 10$; $\alpha = 0.1528$
- 3.11 Plot of pressure at a point on the wave.
 $R_x = 5 \times 10^5$; $a/\lambda = 3 \times 10^{-3}$; $x/\lambda = 10$; $\alpha = 0.1528$

Figure

3.12 Plot of pressure at point 1.

$$R_x = -5 \times 10^5; \quad a/\lambda = 2 \times 10^{-2}; \quad x/\lambda = 10; \quad \alpha = 0.1528$$

3.13 Plot of pressure at point 2 ($\lambda/8$ downstream of point 1).

$$R_x = 5 \times 10^5; \quad a/\lambda = 2 \times 10^{-2}; \quad x/\lambda = 10; \quad \alpha = 0.1528$$

4.1 Evolution of Rayleigh Solutions. A plot of $[(C_{f_o}/C_f)^2 - 1]$ vs T is shown.

4.2 Plot of evolution of solution on a flat plate at Reynolds number $R_{x_o} = 200$ using the periodic Navier Stokes solver. C_f vs Time is plotted. The group velocity of calculations is $C_G = -0.8818/(C_{f_o})^3 \text{ Ku}$

4.3 Plot of evolution of solution on a flat plate at Reynolds number $R_x = 1000$ using the periodic Navier Stokes solver. Both δ^* and C_f variations are plotted. Notice that the data lie in a straight line for the entire evolution cycle.

5.1 Plot of nonplanar geometrics. Fig (5.1a) and (5.1b) are unsymmetric v grooves Fig (5.1c) a symmetric v-groove and (5.1d) a sine waveform of the same amplitude.

5.2 Plot of drag characteristic of nonplanar waveforms in laminar flow as a function of the Reynolds number of oncoming flow.

6.1 Calibration plot of skin friction distribution over a wave cycle of suction and injection distribution for a flow over a flat plate—is no mass transfer --- continuous injection over a cycle ($\lambda = 12''$); -.-, sinusoidal mass transfer using boundary layer code. — -- —, using Navier Stokes solver for the sinusoidal mass transfer case. Notice that the solution using Navier Stokes solver is in excellent agreement with the boundary layer code.

6.2 Plot of drag characteristic for a sinusoidal wave as a function of suction phase angle " ϕ " relative to the wave crest. $\phi = 0$ implies self bleed. Note that drag reduction occurs only for $\phi \sim 180^\circ$ for this case.

Summary

The flow over wave shaped surfaces is studied using a Navier Stokes solver. Detailed comparisons with theoretical results are presented. including the stability of a laminar flow over wavy surfaces. Drag characteristics of nonplanar surfaces is predicted using the Navier-Stokes solver. Also discussed are the secondary instabilities of wall bounded and free shear flows.

Section I

Introduction

At NASA/LaRC there has been an ongoing research program related to flow over wave shaped geometries. The primary objective of this program is to develop surface geometries that have lower aerodynamic drag compared to planar surfaces. This report is an outgrowth of an ongoing computer simulation study of flow over wavy surfaces. The details of the theoretical model and test results of the simulations for both laminar and turbulent flows have already been documented in two previous contractor reports (Ref. 1, 2; NASA CR159305, 1980; NASA CR3408, 1981). Extensive simulation studies that were conducted since then are the topic of the present study.

The problem of flow over wavy surfaces has been a major area of research in fluid mechanics for over a century. The mechanism of wave generation and growth of small amplitude waves in the sea (air-sea interaction) has been a subject of sustained study for many decades. The appearance of ridges in sand dunes is of interest in sediment transport technology (porous wavy surfaces). Small amplitude waviness of machined surfaces and their effect on the performance of aircraft (LFC aircraft for instance) is another application of wavy wall flow phenomena (transition). For sinusoidal wavy surfaces in a narrow band ($a/\lambda \sim 0.03$, $\delta/\lambda \sim 0(1)$) it has been observed experimentally that the wave average skin friction drag in turbulent flow is substantially lower than that of a flat surface. However, the associated wave drag penalty for sine surfaces more than over-compensates for this drag reduction, resulting in a net drag increase for these surfaces. With the availability of high speed computers it has been possible in recent years to solve many intractable problems. Rather than a hit-miss experimental study for low drag

wavy surfaces a reliable computer simulation program (which is economical and accurate) was developed to analyse the total drag properties of both symmetric and asymmetric waveforms. Details of the computer algorithm (Navier-Stokes solver) are given in Ref. 1. Application to turbulent flow and comparison with wind tunnel data are given in Ref. 2.

The present work examines in detail the efficacy of the Miles-Benjamin theoretical model (3) for laminar flows. In Sec. 2, comparisons of laminar flow calculations with theoretical models are presented. In the presence of disturbances, a steady laminar flow undergoes transition at a certain critical Reynolds number. The presence of waviness on the surface can itself produce these disturbances when the wavelength of the surfaces (α) is in the critical range (Sec. 3). For the computer simulation to be effective in rating various geometries (based on their total drag) a proper comparison of methodology is required. Section 4 discusses this concept in detail. In Sec. 5, the results of laminar flow over some low drag surfaces are discussed. The results of drag computations for turbulent flow over a variety of asymmetric and symmetric surfaces are discussed briefly in Sec. 6 with the secondary instability of wall bounded shear flows considered in Sec. 7. A brief discussion of the work carried out in the development of compressible SALLY program under the present contract and work on free shear flows is reported in Sec. 8.

Section II

Laminar Flow Over Wavy Surfaces

Theoretical Models

The simplest model of flow past a wave train is based on the classical Kelvin-Helmholtz theory (4). In this analysis, viscosity is neglected, and the primary flow is uniform. Therefore the disturbance (waviness) can be studied through potential theory. The perturbation pressure on the wave is proportional to the square of the relative velocity between the wave train and the fluid flowing over it and is in antiphase with the wave elevation. Even though this model is naive physically, the pressure component predicted by Kelvin-Helmholtz theory is consistent with the results of a more realistic theory (3) valid for thin boundary layers. ($Re \rightarrow \infty$ or $\delta/\lambda \ll 1$.) Benjamin (3) shows that this pressure component is the only stress remaining in the limit as $Re \rightarrow \infty$ uniformly.

Miles (5) presented an analysis of the wind wave problem considering the inviscid perturbations to a primary profile due to the disturbances. The primary profile has the effects of viscosity (profile curvature) in this analysis. For travelling wave forms where the critical point is away from the boundary a substantial component of pressure in phase with the wave slope (sheltering) may occur. Kendall (6) has experimentally obtained qualitative agreement with Miles theory.

Benjamin's Theoretical Analysis

Benjamin (3) developed a uniformly valid asymptotic analysis of the flow past a wavy boundary. Benjamin's analysis is based on the following assumptions (i) the amplitude 'a' of the wave is much smaller than the wave number k ($=2\pi/\lambda$, where λ = wavelength). (ii) the primary flow is parallel;

i.e. the Reynolds number Re_x is large so that the boundary layer growth over several wavelengths is miniscule, i.e., $U(\eta, \xi) = U(\eta)$ where η, ξ are the normal and tangential coordinates of a point.

The total velocity field is assumed to be derivable from a stream function, i.e.,

$$\psi(\xi, \eta) = \psi_0(\eta) + a\{F(\eta) + (U(\eta) - c) e^{-k\eta}\} e^{ik\xi}$$

where $\psi_0(\eta) = \int_0^\eta [U(\eta) - c] d\eta$ and c is the wave speed of the surface.

The perturbation due to the wave, $F(\eta)$ is influenced by viscosity in a friction layer whose thickness can be evaluated for given flow conditions. This analysis yields expressions for perturbation stresses (pressure and shear stresses) for both laminar and turbulent flow over wavy surfaces.³

Since Benjamin's work a large number of experiments have been conducted over wavy surfaces (turbulent flows). Discrepancies noted between the experimental measurements and theoretical results prompted several workers to develop theoretical models which include perturbation Reynolds stresses (7,8) and solution of the full Navier-Stokes equations (9, 10, 11, 12, 13).

There are very few (reported) laminar flow experiments over wavy surfaces. However, laminar flow calculations serve to calibrate both theoretical and computational methods perhaps better than the turbulent flow case chiefly because of the turbulence closure problem.



Therefore we have performed a number of laminar calculations and compared them to the theoretical model of Benjamin (3).

Navier-Stokes Solver

Our Navier-Stokes solver utilizes conformal mapping and periodic boundary conditions in the flow direction. An inverse stretching extends the computational lid in the normal direction. Under these conditions the unsteady solutions obtained using this code represent the proper physical evolution of the flow. A decided advantage of the periodic code is that, compared to an inflow-outflow code, the periodic code is more economic for problems related to wave trains. Using a Rayleigh analogy concept, which is discussed in Sec. 4, the periodic code has been utilized to study total drag characteristics of various wavy surfaces. Comparison with experiments are presented in Ref. 2. The agreement between the Navier-Stokes simulations and wind tunnel experiments has been satisfactory for the range of geometric parameters and flow parameters tested thus far.

The two dimensional time dependent Navier-Stokes equations are:

$$\rho (\partial u / \partial t + u \cdot \nabla u) = -\nabla p + \nabla \cdot \vec{\tau} \quad (2.1)$$

$$\nabla \cdot u = 0 \quad (2.2)$$

where $\tau_{ij}^+ \equiv \sigma_{ij}$, (which includes both laminar and turbulent stresses for turbulent flows).

The domain of analysis and the appropriate boundary conditions are D :

$$0 < x < 2\pi, f(x,t) \leq y \leq \infty$$

where the wavy surface is

$$y_w = f(x,t)$$

Periodic boundary conditions apply in the flow direction. The boundary conditions appropriate for the normal direction are

$$U(x,0,t) = U_w(x,t)$$

$$v(x,0,t) = V_w(x,t)$$

$$\text{and } U(x,\infty,t) = V(x,\infty,t) = p(x,\infty,t) = 0$$

For a stationary wall

$$U_w = V_w = 0$$

For a wall with normal suction velocity V_w and U_w are nonzero, related to the components of the suction velocity in the physical x, y coordinate directions. Similarly nonzero components of velocity at the wall arise when the wall is moving with a phase speed.

The domain bounded by the wavy surface (5) is mapped to a rectangular $\xi-\eta$ coordinate system using conformal mapping techniques (1) i.e., to the domain D_1 :

$$0 < X < 2\pi, -1 \leq Y \leq +1$$

Initial Conditions

At time $t = t_0$ we prescribe a velocity field appropriate to a starting Reynolds number at the beginning of the wave section., i.e.,

$$\vec{U}(X, Y, t_0) = \vec{U}_0(Y) \quad (2.3)$$

The solution algorithm then develops a quasisteady solution appropriate to the flow over wavy surface.

For laminar flows $U_0(Y)$ will correspond to the Blasius profile appropriate for the starting length. For turbulent flows, a starting profile related to the virtual length of the flow is prescribed. In later sections, (3, 4) the properties of the time evolving flow solutions are related to relevant physical phenomena. For the present, we briefly state that whenever a stable solution for wavy wall flow exists, the solution obtained under these initial conditions and boundary conditions evolved in a fashion similar to the solution over a wave train (with a mean growth of boundary layer thickness due to the downstream length). For instance, the pressure distribution over the first wave will not be quite the same as that a few wavelengths downstream because the flow has a mean boundary layer growth and therefore the surface has a smaller (λ/δ) or (a/δ) . The quasisteady solutions of the Navier-Stokes equation show these variations with time. In section 4, we present a detailed discussion of the evolution in time of the periodic code described herein and evolution of flow over length for an inflow-outflow code over a wavetrain.

For the test problems that are reported herein the results for pressure and skin friction show minimal growth with time mainly because the wavelengths considered are quite small compared to the starting length $(x/\lambda \sim O(10))$. Also, the time of evolution where quasisteady state is reached (related to x in an inflow-outflow code) is quite small for these cases and hence comparisons with Benjamin's theory are appropriate.

Critical Examination of Benjamin's Theoretical Result

Benjamin develops results for rigid walls ($c = 0$) based on three special cases:

(a) Assumption of a linear profile $U(Y) = GY$;

The perturbation stresses are given in (5.6) and (5.7) in Ref. (3) and are written down in nondimensional form (after algebraic manipulations) for a laminar boundary layer as,

pressure:

$$C_p = (2P_s/\rho U_\infty^2) = -.021308 ka R_X^{1/2} (\chi/\lambda)^{-2/3} \{ \cos(kx - \pi/6) + \beta \cos(kx - \pi/3) \} \quad (2.4)$$

shear stress:

$$C_f = (2\tau_s/\rho U_\infty^2) = 0.143806 ka (\chi/\lambda)^{-2/3} \{ \cos(kx + \pi/6) + \beta \cos kx \} \quad (2.5)$$
$$\beta = 3.818 (\chi/\lambda)^{2/3} R_X^{-1/2}$$

Admittedly, the linear profile suffers from a lack of realism. However, when the wavelength of the wall is extremely short, the disturbance would be expected to penetrate only a very small distance away from the wall, where a linear approximation to the velocity profile is justified.

(b) A sinusoidal profile approximating the Blasius profile; i.e.,

$$U = U_\infty \sin KY; \quad 0 < Y \leq \delta \quad (2.6)$$

$$U = U_\infty; \quad Y > \delta \quad (2.7)$$

$$K = (\pi/2\delta), \quad \delta = 5 \chi R_X^{-1/2} \quad (2.8)$$

Benjamin derives expressions for pressure and shear stress, for the case $K > k$ i.e., $\delta/\lambda < 1/4$; the expressions are,

$$C_p = R\ell \frac{[(2ak^2/\ell \times (1 + k/\ell)) \times e^{i(kx + \pi)}]}{[(1 - k/\ell \cot \theta) + 1.288 e^{i\pi/6m/\ell} \times (1 + k/\ell)]}$$

$$C_f = R\ell \frac{[2aK^2 k/\ell m e^{i(kx + \pi/3)} \times (1 + k/\ell)]}{[(1 - k/\ell \cot \theta) + 1.288 e^{i\pi/6m/\ell} \times (1 + k/\ell)]}$$

where $m = (kK\ell_\infty/\nu)^{1/3}$ and $\theta = \ell\delta = \pi/2 \sqrt{1 - (k/K)^2}$

When $\delta/\lambda > 1/4$ the analysis presented by Benjamin can be suitably modified to obtain the expressions for C_p and C_f as

$$C_p = R\ell \frac{[2K^2 a/\ell ((1+n/1-n) + e^{-2\theta}) e^{i(kx + \pi)}]}{[(1+n/1-n) (1.288e^{i\pi/6m/\ell} - 1) + e^{-2\theta} (1 + 1.288e^{i\pi/6m/\ell})]}$$

$$C_f = R\ell \frac{2.746 K^2 ak/\ell m ((1+n/1-n) + e^{-2\theta}) e^{i(kx + \pi/3)}}{[(1+n/1-n) (1.288e^{i\pi/6m/\ell} - 1) + e^{-2\theta} (1 + 1.288e^{i\pi/6m/\ell})]}$$

where $\theta = \ell\delta = \pi/2 \sqrt{(k/K)^2 - 1}$; $n = k/\ell$ and $m = (kK\ell_\infty/\nu)^{1/3}$ **

(c) For the case of a Blasius profile or any general profile, when

$\Delta = (kmU_\infty^2/U'(0)^2) = (km/K^2) \ll 1$, Benjamin develops expressions for C_p and C_f as

$$C_p = R\ell [2k^2 a e^{i(kx + \pi)} (1 - 1.288\Delta e^{i\pi/6}) \int_0^\infty U^2 e^{-kY} dY]$$

$$C_f = R\ell [2.744 k^2 a/m e^{i(kx + \pi/6)}]$$

**For a Blasius profile,

$$K = 0.332 X R_X^{-1/2}, m = 0.20336 k R_X^{1/2} (X/\lambda)^{-2/3}$$

$$\ell = 0.332 R_X^{1/2} / X \sqrt{(358(X/\lambda)^2 R_X^{-1}) - 1},$$

and $\theta = 1.57 \sqrt{358(X/\lambda)^2 R_X^{-1} - 1}$

The implication of these various approximations is now examined.

(i) Assumption of small "ka" limits the accuracy of the solution to small amplitudes.

Benjamin suggests ka should be ≈ 0.02 .

(ii) Assumption of parallel flow requires R_x to be large i.e. — to be of the order of 10. (For $\frac{X}{\lambda} = 10$, the growth of boundary layer over a wavelength is of the order of 5%.)

(iii) Of the three sets of expression that Benjamin develops for a Blasius flow, case (b) seems to be the most appropriate one. Case (a) holds only for very short wavelengths. Case (c) lacks realism as will be shown below. Case (b), where a sinusoidal profile is used to approximate the Blasius profile is a more realistic approximation in that the differences between a sinusoidal profile and a Blasius profile with the same wall slope ($k = \pi/2\delta$; $\delta = 4.73 \sqrt{\nu x/U_\infty}$) are only minimal and should not cause an appreciable difference in the outcome of the results.

The results obtained using case (c) may themselves be of little use. Here the basic requirement for the results to be valid is that the parameters

$$m\delta = 4.2 (KX_0)^{1/3} \gg 1 \quad (2.17)$$

$$\text{and } \Delta = 6.3 (KX_0)^{4/3} R_x^{-1/2} \ll 1 \quad (2.18)$$

The first of these conditions must per-force be met since assumption of parallel flow requires $X_0/\lambda \gg 1$ and hence $KX_0 = 2\pi$ ($k = 2\pi/\lambda$). However the requirement that $\Delta \ll 1$ may not be met for all flow condition. Indeed, an examination of the assumptions carried out to arrive at case (c) one may note that $\Delta \ll 0.1$ or at least of the order of 0.20 for the relation to hold reasonably well. Choosing

a value of $\Delta = 0.2$, we note that,

$$\text{for } X/\lambda = 1, \quad (m\delta = 7.75, \Delta = 0.2) \quad R_X = 1.4 \times 10^5 \quad (2.19)$$

$$\text{for } X/\lambda = 2, \quad (m\delta = 9.8, \Delta = 0.2) \quad R_X = 8.3 \times 10^5 \quad (2.20)$$

(A choice of $\Delta \approx 0.2$ already introduces an error of about 8% in the approximation of the boundary condition (4.8) in Benjamin's paper.)

A choice of $X/\lambda \approx 1$ implies a boundary layer growth of 40% ($X/\lambda \approx 2$ implies a 22.5% change in δ^*) thus violating the assumption of parallel flow. According to our numerical experiments a 40% change in δ^* introduces a change of similar order in the value of pressure due to nonparallelness of the flow. Thus for case (c) to be valid ($X/\lambda > 2$) R_X has to be an unacceptably high value (of the order of millions).

Comparison of Navier Stokes Solutions with Benjamin Theory

In order to verify the appropriateness of Benjamin theory, computer simulations were conducted using the Navier Stokes solver. The results of these calculations are summarized in Tables 1-1 through 1.3 (for a fixed $x/\lambda = 10$).

Table 1.1 presents results for a starting Reynolds number $R_x = 100$; for this case $\delta/\lambda \approx 5.0$. Results are presented for sinusoidal wave amplitudes of 10^{-4} , 10^{-3} , 10^{-2} , 2×10^{-2} , 5×10^{-2} , and 10^{-1} .

Comparison with Benjamin's theory indicates that both the linear profile and the sinusoidal profile approximations show poor agreement with the present computational solution for pressure and shear stress, even for small amplitude waves.

In Table 1.2 we give the results of computer simulations at $R_x = 1000$ with $x/\lambda = 10$. Here again Benjamin's theory and the present Navier-Stokes results exhibit about a 30% difference in pressure amplitude. The sinusoidal profile approximation appears to agree better than the assumption of a linear profile in terms of pressure phase.

In Table 1.3 results are given for $R_x = 10^4$. Here the agreement between theory and simulation is excellent for C_p . The linear profile assumption seems to predict the shear stress distribution better than the sinusoidal profile approximation. This agreement may be fortuitous.

A further aspect that needs to be checked regarding these comparisons is the role of (δ/λ) . Table 1.4 indicates comparisons for various δ/λ 's to obtain a reasonably large δ , we have chosen hypothetical values of $R_x = 10^4$, $U = 10^2$ in/sec $x = 100$ in, etc in the simulations. We have performed two sets of Navier-Stokes calculations here. For $R_x = 10^4$ a Blasius profile is used as the starting profile in the first set of calculation and for the second set the oncoming flow is taken as a shear flow with the same $U'(0)$ at the wall as the Blasius profile. [In the freestream i.e., $y > 1/\kappa$ (where $\kappa = U'(0)/U_\infty$) the velocity is kept $= U$, and for $y \leq 1/\kappa$, $U = u'(0)y$.]

It is seen that the Navier Stokes solutions differ from each other by 10%. This is to be expected due to the difference of profile shapes. However Benjamin's theoretical predictions do not agree with the Navier Stokes solution. For $\delta/\lambda = 1.0$ both the sine and linear approximation agree within 10% in amplitude. For larger values of δ/λ the discrepancy is greater.

We conclude from these numerical studies that the asymptotic theoretical results are evidently not accurate for moderate Re .

Consideration of Couette Flow Assumption for Navier Stokes Solvers

A number of works (theoretical methods and Navier-Stokes solvers) (Refs. 9,10, 11) utilize a shear flow assumption for the unperturbed flow. These computer algorithms use periodic inflow and outflow condition with a moving lid at the top. For this case it is well known that a true steady state is available.

It is, therefore, interesting to examine how well these codes may perform in the prediction of developing flow over a wavy wall.

Since the flow is assumed to be a high Reynolds number flow, there should be no dependence on development length (X_0). Thus the characteristic Reynolds number is $R_\lambda \approx U_\lambda \lambda / \nu$ where U_λ is chosen as a velocity scale at a distance λ from the wall ($U_\lambda = \kappa \lambda$ where κ is the velocity gradient at the wall). We observe from Table 1.4 that a linear profile for the primary flow produces an error of about 10% in results when compared to the Blasius profile whenever the wall velocity gradient is chosen the same for both cases (see the Navier Stokes results of Table 1.4). Since the wall velocity gradient of a laminar flow at a Reynolds number $R_x = U_\infty X / \nu$, is given as

$$U'(0) = 0.332 U_\infty / \sqrt{R_x} = 0.332 U_\infty / X R_x^{1/2} \quad (2.21)$$

this must be equated to κ in order to make an appropriate couette flow approximation of the developing boundary layer.

$$\text{Thus} \quad \kappa = 0.332 U_\infty / X R_x^{1/2} \quad (2.22)$$

$$\begin{aligned} \text{and } R_\lambda = \kappa \lambda^2 / \nu &= 0.332 U_\infty \lambda^2 / \nu X R_x^{1/2} \\ &= 0.332 R_x^{3/2} (X/\lambda)^{-2} \end{aligned} \quad (2.23)$$

Therefore a Couette flow Reynolds number R_λ corresponds to a Reynolds number

$$R_x = 2.0856 R_\lambda^{2/3} (X/\lambda)^{4/3} \quad (2.24)$$

In Table 1.5, for a given $R_\lambda = 5000$ and waveheight $a/\lambda = 10^{-3}$, we have performed calculation of C_{p0} and ϕ for various (X/λ) 's. [For $R_\lambda = 5000$ and $X/\lambda = 1$ Eqn. (2.24) gives $R_x = 609.8$; for $X/\lambda = 2.0$ $R_x = 1537$; and for $X/\lambda = 4$, $R_x = 3872$.]

If the couette flow results are to be meaningful, the C_p values should agree with one another. In reality they vary widely depending on the value of R_x or x/λ . The implication is that it is not the shear flow assumption itself that is at fault, but the denial of the memory to the fluid (development length) by virtue of defining R_λ .

Influence of Surface Waviness on Flow Stability

Laminar flows are subject to instabilities and eventual transition to turbulence at large Reynolds numbers. At very low Reynolds numbers disturbances introduced into the flow decay with time. When the Reynolds numbers are above the critical Reynolds number ($Re_* = 520$ on a flat plate) small amplitude disturbances may grow in time depending on the nature of the disturbance (wavenumber or frequency). This is an eigenvalue problem i.e.

$$F(\alpha, \omega) = 0 \quad (3.1)$$

where α is the wavenumber and ω is the angular frequency (complex number). The initial growth of a small amplitude disturbance can be studied using the parallel flow assumption for the primary flow. The equation system governing the disturbances is the classical Orr-Sommerfeld equation

$$(D^2 - \alpha^2)^2 \Phi = i\alpha R [(U - c)(D^2 - \alpha^2)\Phi - U''\Phi] \quad (3.3)$$

In general, Squire's theorem states that three dimensional disturbances are typically less disruptive than the two dimensional disturbances small amplitude fluctuation in incompressible flow.

The linear growth regime of small disturbances had been studied exhaustively (6) for flat plates. In general, the source of the initial disturbance is very difficult to control even under rigorous laboratory conditions. Abrupt or drastic changes in surface geometry (trips, roughness) sound sources in the field or even freestream vorticity can provide the initial disturbance which causes the flow to undergo transition.

We next examine the subsequent disturbance growth behavior for a disturbance free stable laminar flow on a flat plate encountering a wavy wall of a given amplitude and wavelength.

In section (2.4) we stated that the solution of the Navier-Stokes equations was obtained for flow over a wavy surface with a starting velocity profile, i.e. a Blasius profile at time $t = t_0$,

$$\text{i.e.,} \quad U(X, Y, t_0) = U_0(Y, t_0) \quad (3.4)$$

Once the calculations begin, a perturbation field is generated due to the change in geometry. For instance, the perturbation to U_0 at $(t_0 + \Delta t)$ is at most of the order $(ka\Delta t)$ where the wall has a wavenumber $'k' = 2\pi/\lambda$. For the next few time units the flow has to undergo an adjustment towards the eventual velocity profile $U(X, Y, t)$ appropriate for the wavy surface. We note that Benjamin, using asymptotic theory, has shown that the perturbations from a mean flow over a wavy surface with $a \ll 1$, and $ka \ll 1$ satisfies the Orr-Sommerfeld type equation ((see 3.1) of Ref. 3). The solution of the Navier-Stokes equation at early times can therefore be viewed as perturbations with the wavenumber $'k'$. Therefore it is reasonable to expect that the solution at initial times of the unsteady Navier-Stokes solver can be studied to get information regarding the stability of the flow.

Results of Computer Experiments

When the Reynolds number of the oncoming flow is well below a critical value the presence of waviness does not affect the stability of the flow. As an illustration the plot of pressure at a point with time (non-dimensional with $\lambda/2\pi U_0$) is shown in Fig. 3.1. The calculations were performed under the following conditions: $X_0 = 1000$, $\lambda = 12$, $U_0 = 10$, $a/\lambda = 10^{-3}$. The initial adjustment time from the figure is roughly 24 units.

Since small amplitude perturbations of the Orr-Sommerfeld equations travel at a speed of roughly $0.2-0.25 U$ at these low Reynolds numbers, this time corresponds to a traversed distance of one wavelength for the perturbation.

$$[24 \times (.25 U_0) \times (\lambda/2\pi U_0) \approx \lambda]$$

After a time of 24 units the pressure shows a slight decay with time. This decay has been found to be strictly proportional to the growth of the boundary layer in all of our calculations, i.e., $\Delta\delta^*/\delta^* \approx \Delta p/p$. For the problem considered $\Delta\delta^*/\delta^* = 1.8\%$ and $\Delta p/p \approx 4/438 \approx 1\%$.

In Fig. 3.2 a plot of the pressure at a point is presented for the case $R_X = 10^4$, $X = 10^3$, $\lambda = 60$. Again one can observe that the initial transient settles down by a time $t = 30$ units. The decay of the pressure for subsequent times can again be compared to growth of the boundary layer. From the figure we deduce that the boundary layer grows by $\Delta\delta^* \approx 8.6\%\delta^*$ and the pressure decays by $\Delta p = 11.7\%p$.

When the Reynolds number of the oncoming flow is near the critical value the pressure transients show different patterns. Figs. 3.3 through 3.9 show the behaviors of the pressure transient with time for an oncoming Reynolds number $R_X = 10^5$ ($X_0 = 10^4$, $U_0 = 216"/\text{sec.}$) and various wall wave combinations.

Figure 3.3 presents results for a wall valve of amplitude $\alpha = 5 \times 10^{-4}$ with a wavelength $\lambda = 2$ ". The nondimensional wavenumber $\alpha = \frac{2\pi\delta^*}{\lambda}$ for this case is $\alpha = 0.1709$. The pressure transient contains a mean component which decays with time along with a Tollmein-Schlichting wave which behaves like a damped oscillator. Notice that the successive maxima are equally spaced in the time domain. The mean line dividing the envelope of maxima and minima for this case is the true mean pressure due to the wavy surface. The period of separation between successive maxima for this case is $\tau_0 = 18$ units. [$t_0 = \tau_0 \lambda / 2\pi U_\infty$ and hence $\omega_r = 2\pi/t_0 = 4\pi^2 U_\infty / \lambda \tau_0$.] Thus the nondimensional frequency $\omega_r \delta^* / U_\infty = 0.0596$ give $c_r = \omega_r / \alpha = 0.349 U_\infty$, the velocity of propagation of the T-S wave. The logarithm of the ratio of successive maxima yields $\omega_i \tau_0$. For this case $\omega_i \delta^* / U_\infty = -4.4 \times 10^{-3}$. A separate Orr-Sommerfeld calculation for a linear perturbation to the flow at $R_x = 10^5$ gives the value

$$\frac{\omega_r \delta^*}{U_\infty} = 0.0590 \quad ; \quad \frac{\omega_i \delta^*}{U_\infty} = -4.226 \times 10^{-3}$$

Figures 3.4 and 3.5 show plots of pressure transient at two points separated in space by a distance $\lambda/8$, for the case $a = 1 \times 10^{-3}$, $\lambda = 1$ " ($R_x = 10^5$, $X = 10$ ", $U_\infty = 216$ " / sec). The nondimensional wavenumber $\alpha = 2\pi\delta^* / \lambda = 0.34175$ for this case. The successive maxima and minima are separated by a time period of 16 units, yielding $\omega_r = 533$ rad/sec or $\omega_r \delta^* / U_\infty = 0.1363$; for this case $\omega_i \delta^* / U_\infty = -7.5 \times 10^{-3}$. The velocity of propagation $c_r = 0.399 U_\infty$. By comparing Figs. 3.4 and 3.5 it is seen that the pressure signal in (3.5) is shifted by a time unit $\tau_1 = 2$ units from that in (3.4). Thus

$$\lambda/8 = c_r \tau_1 \quad \text{giving} \quad c_r = \pi/8 U_\infty = 0.393 U_\infty$$

Solution of the Orr-Sommerfeld equation yields

$$\omega_r \delta^*/U_\infty = 0.13743 \quad ; \quad \omega_i \delta^*/U_\infty = -2.1865 \times 10^{-4}$$

In fig. 3.6 a plot of pressure transient for a wall wave of amplitude $a = 5 \times 10^{-3}$; $\lambda = 1''$ is given ($R_x = 10^5$, $X = 10''$, $U_\infty = 216''/\text{sec}$). From the figure $\omega_r = 523 \text{ rad/sec}$ $\omega_r \delta^*/U_\infty = 0.132$ and $\omega_i \delta^*/U_\infty = -7.92 \times 10^{-3}$ and $c_r = 0.386 U_\infty$

For Fig. 3.7 the amplitude of the wave wall was increased to $a = 1 \times 10^{-2}$ in. The separation between successive maxima no longer display constancy in period. even though they are approximately equal. Indeed the nonlinear nature of the wave is barely observable (shorter fetch during rise and longer fetch during fall in the oscillation in the initial phases of the oscillations).

In Fig. 3.8, the pressure transient for a wall wave of amplitude $a = 3 \times 10^{-2}$ in, $\lambda = 1''$ ($R_x = 10^5$, $X = 10''$, $U = 216''/\text{sec}$) is plotted. Notice the growth of the pressure perturbation with time.

In Fig. 3.9 the pressure transient for a wall wave of $a = 5 \times 10^{-2}$ in ($\lambda = 1$, $R_x = 10^5$) indicates the essentially nonlinear nature of the growth of the disturbances. For both (3.8) and (3.9) stable quasilinear solutions are not available indicating the time unsteady separation of the flow in the wall region [the solutions indicate the growing nature of the separation bubble eventually leading to complete breakdown of the flow at a later time].

In Figs. (3.10) through (3.13) the flow conditions are $R_x = 5 \times 10^5$; $U_\infty = 1080''/\text{sec}$, $X = 10''$. The wavelength of the wall wave is chosen as $\lambda = 1.0''$.

Fig (3.10) shows plots of pressure for a wave amplitude $a=1 \times 10^{-3}$. From the figure, $\alpha = 0.1528$; $\omega_r \delta^*/U_\infty = 0.04796$; $\omega_i \delta^*/U_\infty = -2.9 \times 10^{-3}$ and $c_r = 0.314$. The Orr-Sommerfeld solutions yield $\omega_r \delta^*/U_\infty = 0.046275$; $\omega_i \delta^*/U_\infty = -2.097 \times 10^{-4}$ for this case.

In Fig. (3.11) the amplitude of the wall wave is $a = 3 \times 10^{-3}$. At this amplitude itself the nonlinear effects are barely visible.

Fig. (3.12) depicts the situation for the case of wave amplitude $a = 1 \times 10^{-2}$. The wave form now consists of a group of traveling waves. This is obtainable by considering Fig. 3.12 along with Fig. 3. 13 where the pressure signal at a point $\lambda/8$ downstream is plotted. The constant phase shift can be converted to obtain the group velocity $C_G \approx 0.26 U$. At higher amplitudes a total breakdown of the flow is noticable in convective time scale of $O(1)$.

Methodology for Evaluating the Drag Reduction Characteristics of Wavy Surfaces

In a wind tunnel the drag reduction characteristics of various nonplanar surfaces may be compared by measuring the total drag forces on the surface and comparing these to a planar surface. When numerical simulations are used to evaluate the drag characteristic of various nonplanar surfaces, the following requirements must be satisfied: (1) The simulation should be highly accurate and capable of predicting the skin friction and pressure drag on the surface accurately. (2) The simulation should be more economical than the experimental work.

The Navier-Stokes algorithm reported in (Refs. 1 and 2) satisfies both these criteria. The Fourier Spectral method has been found to predict the total drag on wavy surfaces in turbulent flow in agreement with experiments (Ref. 2). The algorithm reported in (Refs. 1 and 2) uses periodic boundary conditions in the flow direction. While this has a decided advantage in terms of cost effectiveness as compared to an inflow/outflow steady state solver (spatial), there is a nagging doubt with regard to the accuracy of the solution vis a vis the inflow-outflow codes. The results that are reported herein should provide some answers to these doubts.

We note that the inflow-outflow codes can be a burdensome asset when flow over more than one wave (multiple waves) needs to be studied. For each wave a resolution of at least 30 points are needed in the wave-direction (in order to estimate phase of pressure distribution with an accuracy better than 5°) thereby increasing computation time as well as storage requirements.

Secondly, conformal mapping techniques become prohibitively expensive to employ for these problems because a flow over N waves increases the computational labor N fold due to mapping complexity. A spatial code in these situations is less desirable than a properly constructed temporal code. The Navier Stokes solver described in Sec. 2 is a temporal code. In order to correlate the temporal evolution of solution to spatial evolution of a developing flow, we consider the following three illustrative examples:

1) Consider at time $t = t_0$, a flat plate which is set suddenly in motion with a velocity $U = -U_0$. By Galilean transformation this is equivalent to the flow surging at $U = U_0$ at $t = t_0$ and the plate stationary at subsequent times (a classical Rayleigh problem.) For this problem the governing equation of motion is

$$\partial u / \partial t = \nu \partial^2 u / \partial y^2 \quad (4.1)$$

with, at $t = 0$: $U = U_0 \quad y > 0$

$$U = 0 \text{ at } y = 0$$

and $U = 0$ at $y = 0$ at all times.

The solution for velocity, shear stress, etc. is

$$U = U_0 \operatorname{erf} y / \sqrt{4\nu t} \quad (4.2)$$

and $\tau_w = U_0 \sqrt{\mu \rho / \pi t} \quad (4.3)$

where $\operatorname{erf}(z) = \frac{2}{\sqrt{\pi}} \int_0^z e^{-\xi^2} d\xi \quad (4.4)$

A Reynolds number can be constructed for the flow as,

$$Rr = U_{\infty}^2 t / 4\nu \quad (4.5)$$

The displacement thickness δ_1 for the flow is

$$\delta_1 \approx 1.99 (U_{\infty} t) / \sqrt{Rr} \quad (4.6)$$

and the skin friction

$$C_f = 0.5624 / \sqrt{Rr} \quad (4.7)$$

For a developing Blasius flow the relations are

$$\delta_1 = 1.72 X / \sqrt{R_X} \quad (4.8)$$

$$\text{and } C_f = 0.664 / \sqrt{R_X} \quad (4.9)$$

Because of the difference in the numerical constants in (4.5) through (4.9) a proportionality between X and τ is not strictly correct. (An error of 10% occurs for skin friction values if the relation $X = U_{\infty} t / 2 = C_{G1} t$ is used for Rayleigh analogy.) If, however, a velocity scale is chosen such that $C_{G2} = .664 / .5624$ $C_{G1} \approx .6 U_{\infty}$ the Rayleigh solutions give reasonably accurate values for various profile parameters. Thus even for this problem a meaningful analogy can be constructed.

In Fig.4.1, a plot of $[(C_{f_o} / C_f)^2 - 1]$ vs T is shown. The solutions were obtained using the periodic Navier Stokes Solver with amplitude of wave $a = 0$ and with the initial condition given by (4.1).^{*} Our calculations give $C_{G2} \approx 0.62 U_{\infty}$, in good agreement with the exact solution.

^{*}The group velocity of computation can be determined by using the formula, $C_{G2} = [0.4409 K\nu / (C_f U_{\infty})^2] U_{\infty}$ where K is the slope of the curve shown in Fig. 4.1.

To investigate the nature of the solution with time the following initial conditions are prescribed
 $t = t_0$: $u = U(Y)$, where $U(Y)$ is the Blasius profile corresponding to some x Reynolds number R_{X_0} .

Since the equation system (4.1) does not have an x dependence at $t = t_0$, the solution at all times will also be x -independent. Because of the parabolicity of (4.1) at large times the solution tends to the Rayleigh solution. Of interest, however, is the nature of the solution at small and intermediate times. In the small to intermediate times memory of the initial profile exists for the flow.

We illustrate this behavior for the solution through Fig. (4.2) and (4.3), where R_{X_0} of 200, 1000 are chosen in the examples. The group velocity of computation C_G is equal to 0.21, which is the perturbation speed of propagation at these Reynolds numbers.* The time domain in Figs. (4.2) and (4.3) is normally the time taken to obtain a quasisteady solution for a wavy wall of the same periodic length as the computational box.

There is hardly any scatter of data points from the straight line in these figures. This means that the solution of the flat plate at different times ($t_0 + t_1$) can be related to the solution for a developing boundary layer at $X_0 + x$, where $x_1 = C_G t_1$. This concept is of crucial interest in developing a methodology for rating the drag characteristic of various nonplanar surfaces.

*The group velocity of computation can be determined by using the formula, $C_{G_2} = [0.8818 K \sqrt{C_f U_\infty^2}] U_\infty$ where K is the slope of the curves shown in Figs. 4.1-4.3.

The approach that we have adopted for drag comparisons is to start a wavy wall calculation at time T_0 with a Blasius profile corresponding to an X Reynolds number R_{X_0} . At various time intervals $(t_0 + n\Delta t)$ the total drag of the wavy surface is computed. These quasisteady values are compared to the local skin friction coefficient value at $(X_0 + nC_G\Delta t)$ in order to obtain a reasonable comparison of the performance of various surfaces.

Nonplanar Surfaces for Drag Reduction in Laminar Boundary Layers

Turbulent flow covers much of the surface area on CTOL aircraft. However, the residual areas of laminar flow (e.g., near nacelle leading edges and the fuselage nose region) can contribute large skin friction drag levels due to their initially low Reynolds number. Research reported herein indicates that certain nonplanar geometries can reduce net skin friction drag, even in laminar flows. Thus nonplanar waveforms may be a viable alternative to the more esoteric technique of laminar drag reduction through "supersmooth" ("slip" boundary) surfaces. A computer simulation technique (Navier-Stokes Solver) using high order numerical methods has already been developed for both laminar and turbulent flow wavy wall cases (Ref. 1,2) and it was found that the computer simulations accurately predict (for turbulent flows), within a 4 percent error margin, drag levels measured in the wind tunnel.

In the laminar flow region the prediction capability of the present code is further improved due to the obvious absence of turbulence modeling and associated inaccuracies. Fig. 5.1 indicates four waveforms with $a/\lambda = 0.2$. Calculations of total drag for these waveforms were conducted in the Reynolds number range $R_x = 100$ to 1000. The variation of total drag as compared to flat plate drag is shown in Fig. 5.2. The unsymmetric V-groove of Figure 5.1a was found to have a net 17 percent drag reduction compared to a smooth flat surface with the same planform area. The sine waveform was shown to have a drag penalty starting with the lowest Reynolds number.

Our conclusions are that, at least at low Reynolds number, certain nonplanar asymmetric waveforms may perform better than a smooth flat plate. The mechanism of viscous drag reduction is the nonlinear effect of the pressure distribution over these waveforms. The asymmetric shape of the surface is crucial in providing a net drag reduction. Only in certain cases (Figs. 5.1a,b) is the associated pressure drag on the wave smaller than the skin friction reductions. These studies are ongoing, with emphasis upon higher Reynolds number and further surface optimization.

The Effect of Suction and Injection on the Total Drag of a Wavy Surfaces

The increased cost of fuel has reemphasized viscous drag reduction research. The skin friction reduction obtained through surface mass injection is well known. However, the effect of spatially non-uniform surface injection on the amount of drag reduction (with fixed mass flow rate) has not been examined in detail. An interesting approach to providing local (passive) mass sources and sinks is the use of a porous wavy-wall configuration with its alternating pressure levels to provide self-induced mass transfer through the porous wall. In this case the pressure distribution over the surface wave can result in a non-negligible pressure drag which may be a significant part of the total drag on the surface. The purpose of the present study was to examine theoretically the effects of various spatial variations of suction and injection on the drag of both flat and wavy surfaces.

Calculations have been made for two (four foot long) surfaces, one flat and the other sinusoidal with a wave length of one foot. In each case the undisturbed velocity was 50 fps, the initial boundary layer was turbulent at $R_0 = 4500$, and the initial boundary layer thickness was approximately 1.8 inches. These conditions correspond to the experiment of Sigal for a wavy-wall with no suction or injection¹⁴. For the flat surface, a finite-difference boundary layer code described in Ref (15) was used to determine if spatial variations in mass transfer for a fixed total flow rate could result in enhanced drag reduction. This code was used previously¹⁶ to study the effect of Mach number on drag reduction due to uniform surface

injection. For the sinusoidal surface, calculations were made using the Navier-Stokes code for a sinusoidal distribution of suction and injection perpendicular to the wall. In both programs modelling constants of $k = .41$ and $(\ell/\delta)_{\max} = .085$ were used in zero order (mixing length) turbulence closure schemes, and the wall damping factor, A^+ , was assumed to be the following function of V^+ for low speed flow :

$$A^+ = 26 \exp(-5.9 V^+) \quad (1)$$

A number of works^{8, 13} have suggested using $A^+ = f(P^+)$ and $k = f(\rho)$ corrections as a means of including the equilibrium effects of pressure gradient on turbulence. However, computations reported in Ref. 2 indicated that the pressure and skin friction distributions over Sigal's wave could be adequately predicted using zero pressure gradient constants (probably due to the nearly "frozen" nature of the turbulence structure); therefore, no corrections of the type proposed in Refs. 8 and 13 were applied in the present calculations.

The Navier-Stokes code was tested by comparing calculations on a flat surface with a sinusoidal distribution of injection and suction ($v_w/u_\infty = .005$ at maximum suction and injection) to similar calculations made with the boundary layer code. Results obtained for an impermeable wall, a flow with constant blowing, and the sinusoidal suction solution for one cycle of suction and blowing are shown in Fig. 6.1. The drag coefficient calculated for the surface element (four cycles of suction and injection) was 2.86×10^{-3} from the boundary layer code and 2.81×10^{-3} from the Navier-Stokes code. Note that the integrated skin friction drag over the region where the sinusoidal suction was applied is greater than the drag of an impermeable surface.

In Fig. 6.2, the Navier-Stokes calculation for a sinusoidal wave ($h = 0.01''$, $\lambda = 12''$, $\delta = 3''$) with suction velocity $(v_w/u_\infty)_{\max} = .003$ is presented. From the figure it is apparent that the self bleed situation ($\phi = 0^\circ$) imposed a substantial drag penalty over that of a wavy surface with no mass transfer, mainly through an increase in pressure drag (phase shift). The opposite situation occurs for peak suction at the crest ($\phi = 180^\circ$). Here the reduction is mainly due to a pressure thrust. Calculations were also made with different peak suction rates for the same wave. All these calculations indicate similar trends with ϕ . However, there seems to be a critical $(v_w/u_\infty)_{\max}$ for a given wave and flow conditions for which the total drag reduction is a maximum when $\phi \approx 180^\circ$. Above this critical value the total drag goes up for all ϕ . It may thus be possible to obtain a total drag reduction over the wavy surface by a suction distribution with $\phi \approx 180^\circ$. However, the associated penalty for collecting and ducting the flow (which is not considered in this analysis) implies that this is not a desirable option for drag reduction on sine waves. The original possibility which prompted the study, that of using passive bleed over the wave, is seen to be detrimental.

Drag Characteristics of Nonplanar Waveforms in Turbulent Flow

The Navier Stokes solver discussed in Ref. 1 and 2 has been used to study the drag characteristics of various nonplanar waveforms in turbulent flow. For turbulent flows closure of the time average Navier Stokes equations is required. In Ref. 2, various closure models have been tested. It may be recalled here, that, based on the available experimental data, the zero equation model with equilibrium constants performs adequately in flow predictions for nondimensional amplitudes of ka up to ≈ 0.2 . [The experiments against which comparisons were made in Ref. 2 are (i) Kendall's experiment ($ka = 0.19$, $R_0 \approx 2000$), (ii) Sigal's experiment ($ka = 0.17$, $R_0 \approx 6000$) (iii) LaRC inhouse experiments in the 7 x 11 tunnel ($R_0 = 2000$, $ka = 0.03$ - 0.125 , with sine waveforms and other nonplanar waveforms.)] The design studies that are given here, therefore, use the zero equation closure model ($(\ell/\delta)_{\max} = 0.09$; $K = 0.4$; $A^+ = 26.0$). The methodology discussed in Sec. 4, is used to determine the drag characteristic of the nonplanar waveforms: i.e., the evolution of the solution over the nonplanar waveform is compared to the evolution over a flat surface. The design studies are purposely made for the 7" x 11" tunnel conditions of LaRC so that "promising" candidate surfaces can be tested at a later date. (These experiments are currently underway.)

Based on the results of earlier experiments it was observed that symmetric sinusoidal waves have higher form drag penalties compared to other waveforms of the same wavelength and amplitude. The purpose of this study was to compute various asymmetrical surface shapes and study their overall drag characteristics.

In the following we report the results of our investigation. It was noted in Sec. 4 that the convection speed of the

calculations (i.e., C_G) for turbulent flows was approximately $C_G \approx 0.8U_\infty$. The initial (startup) transients decay at a time scale smaller than for laminar flows. In fact, we note that the skin friction and pressure distributions settle down after 4 units of non-dimensional time $(4(\lambda/2\pi U_\infty)\text{sec})$ i.e., in a time required for the box to float a distance $\approx 0.5\lambda$.

In the following we briefly describe the surface waveforms drag characteristics.

(1) Initial (Flat Plate) Results

The results of computer solutions for a flat plate at 7" x 11" conditions ($U_\infty = 75"/\text{sec}$, δ initial = 0.375") at various time evolutions (non-dimensional time) are presented below.

Time	3.0	3.6	4.2	4.8	5.4	6.0
$C_f \times 10^3$	3.707	3.675	3.643	3.614	3.587	3.563
R_θ	2687	2691	2694	2698	2702	2706

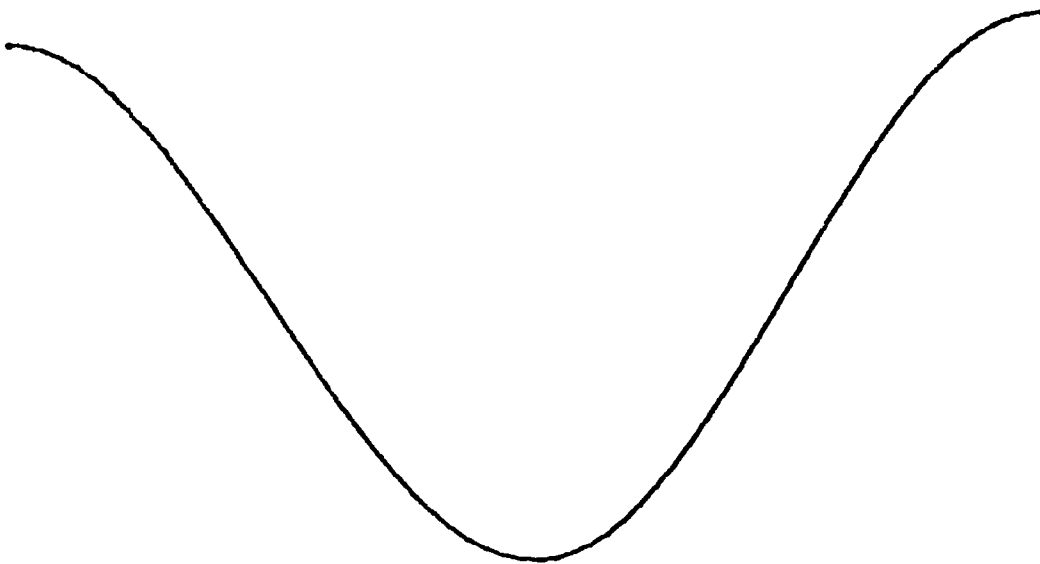
Entry B1

Surface: sine wave, $a = 0.03''$, $\lambda = 1''$ ($ka \approx 0.188$)

Results of the simulations are

Time	3.6	4.2	4.8	5.4	6.0
$C_{D_f} \times 10^3$	3.645	3.585	3.528	3.475	3.428
$C_{D_p} \times 10^3$	2.209	2.027	1.985	1.988	1.996
$C_{D_T} \times 10^3$	5.851	5.613	5.513	5.463	5.424
% Drag Change	59.2%	54.1%	52.5%	52.3%	52.3%

There is a drag increase of 52% for this wave which is mainly due to the pressure drag on the surface (form drag \approx 56% of the flat plate).



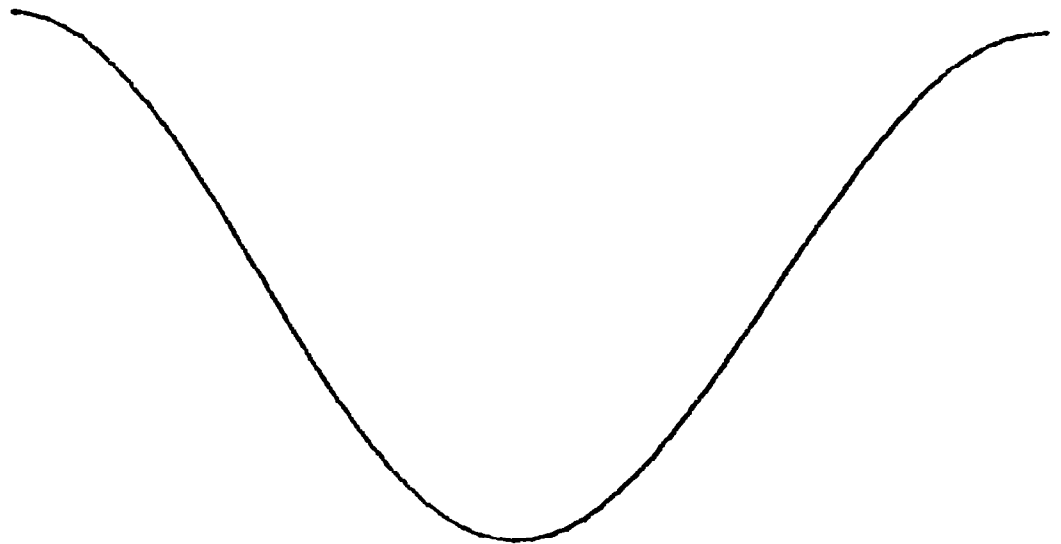
Entry B2

Surface: sine wave, $a = 0.015''$, $\lambda = 1''$ ($ka \approx 0.10$)

Results are tabulated below

Time	3.6	4.2	4.8	5.4	6.0
$C_{D_f} \times 10^3$	3.665	3.626	3.590	3.556	3.524
$C_{D_p} \times 10^3$	0.574	0.528	0.510	0.504	0.502
$C_{D_T} \times 10^3$	4.239	4.154	4.100	5.060	4.026
% Drag Change	15.35	14.0	13.4	13.2	13.0

Notice that once again the form drag on the surface is greater than frictional drag reduction on the surface.

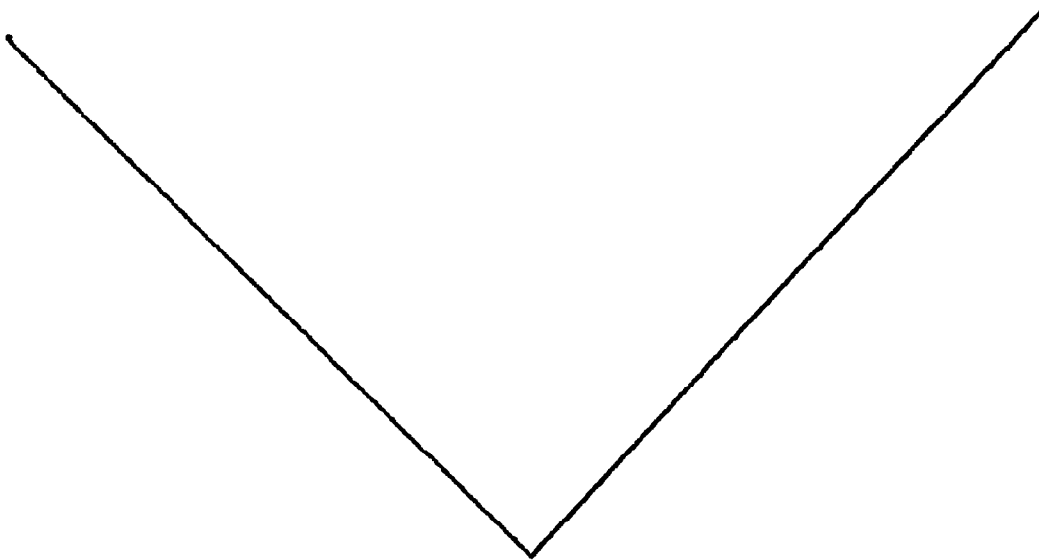


Entry B3

Surface: symmetric V groove, $a = 0.015''$, $\lambda = 1$

Time	3.6	4.2	4.8	5.4	6.0
$C_{D_f} \times 10^3$	3.644	3.597	3.553	3.512	3.474
$C_{D_p} \times 10^3$	0.432	0.400	0.388	0.383	0.380
$C_{D_T} \times 10^3$	4.076	3.997	3.941	3.895	3.854
% Drag Change	10.9	9.7	9.05	8.59	8.17

It is noted that the form drag is about 25% less than that for a sine wave of the same amplitude (compares to entry B2).



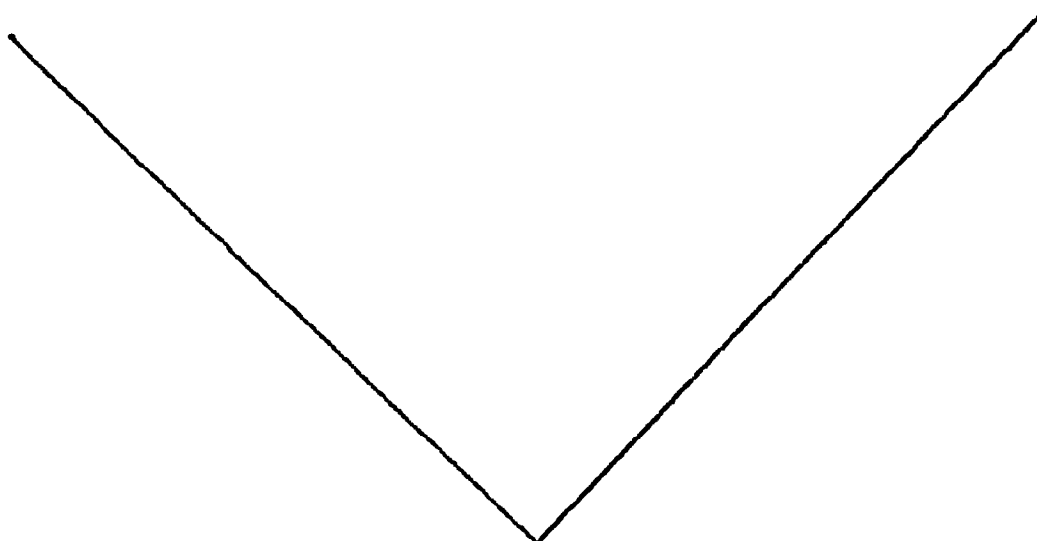
Entry B4

Surface: symmetric V groove, $a = 0.0236$, $\lambda = 1''$

(The V-groove has the same wall slope as the maximum slope on a sine surface (i.e., Case B2) for this case.)

Time	3.6	4.2	4.8	5.4	6.0
$C_{D_p} \times 10^3$	3.600	3.535	3.472	3.413	3.357
$C_{D_p} \times 10^3$	1.077	1.005	0.979	0.974	0.974
$C_{D_T} \times 10^3$	4.677	4.54	4.45	4.387	4.331
% Drag Change	27.3	24.6	23.2	22.3	21.5

Note that the pressure drag is proportional to a^2 for a given k . Our simulation (compare B3 and B4; B1 and B2) attest to this.



Entry B5

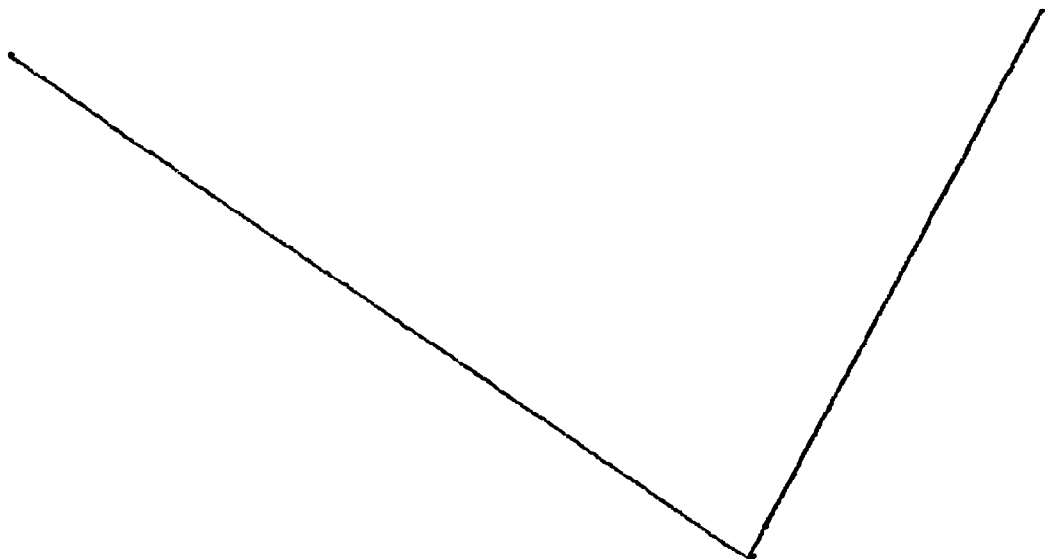
Surface: unsymmetric V-groove, $a = 0.015''$, $\lambda = 1''$

The unsymmetric V groove can be analytically described as;

$$y = a(1 - 2.857 x/\lambda) \quad 0 < x/\lambda \leq 0.7$$

$$y = a(6.67 x/\lambda - 5.67) \quad 0.7 \leq x/\lambda \leq 1.0$$

Time	3.6	4.2	4.8	5.4	6.0
$C_{D_f} \times 10^3$	3.649	3.604	3.561	3.521	3.484
$C_{D_p} \times 10^3$	0.446	0.409	0.388	0.376	0.366
$C_{D_T} \times 10^3$	4.096	4.013	3.950	3.897	3.850
% Drag Change	11.45	10.20	9.30	8.64	8.05



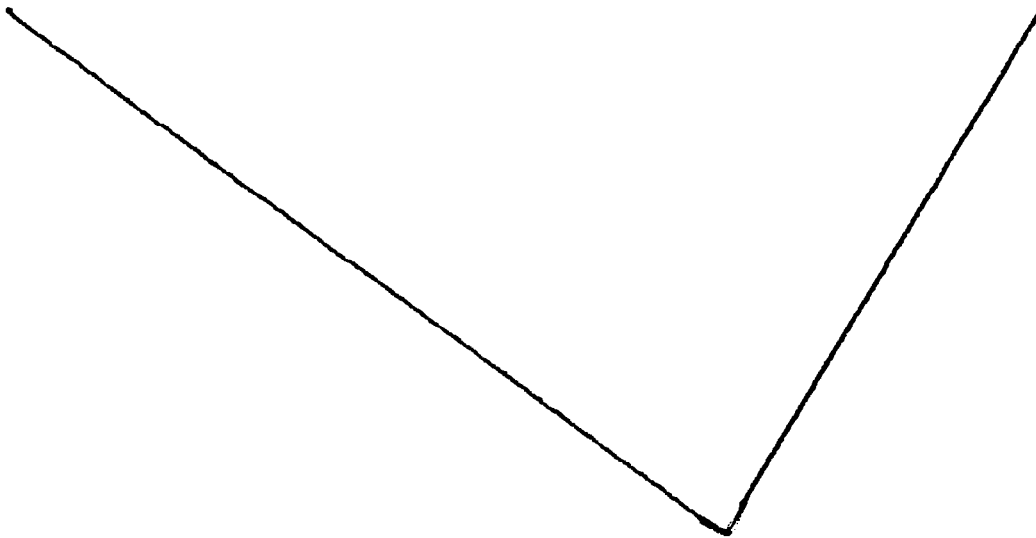
Entry B6

Surface: unsymmetric V-groove, $a = 0.03''$, $\lambda = 2''$

The surface has the same shape as Entry B5

Time	3.6	4.2	4.8	5.4	6.0
$C_{D_f} \times 10^3$	3.499	3.455	3.418	3.386	3.359
$C_{D_p} \times 10^3$	0.436	0.376	0.336	0.307	0.284
$C_{D_T} \times 10^3$	3.935	3.831	3.754	3.692	3.644
% Drag Change	7.0	5.16	3.88	2.93	2.27

There is a 20% reduction in form drag solely due to δ/λ variation (compared to B5)

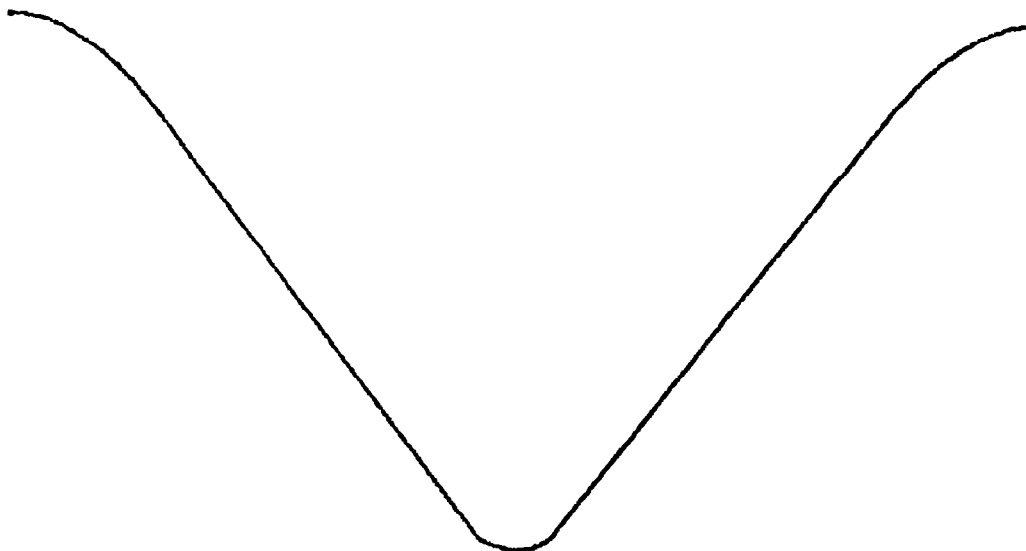


Entry B7

Surface: symmetric rounded and straight shape.

The surface can be described best as follows. The crests have a convex curvature $\kappa = 0.5/\text{in.}$ and the troughs have concave curvature $\kappa = 1.0/\text{in.}$ The rounded portions are connected by straight line segments; $a = 0.015''$ $\lambda = 1''$.

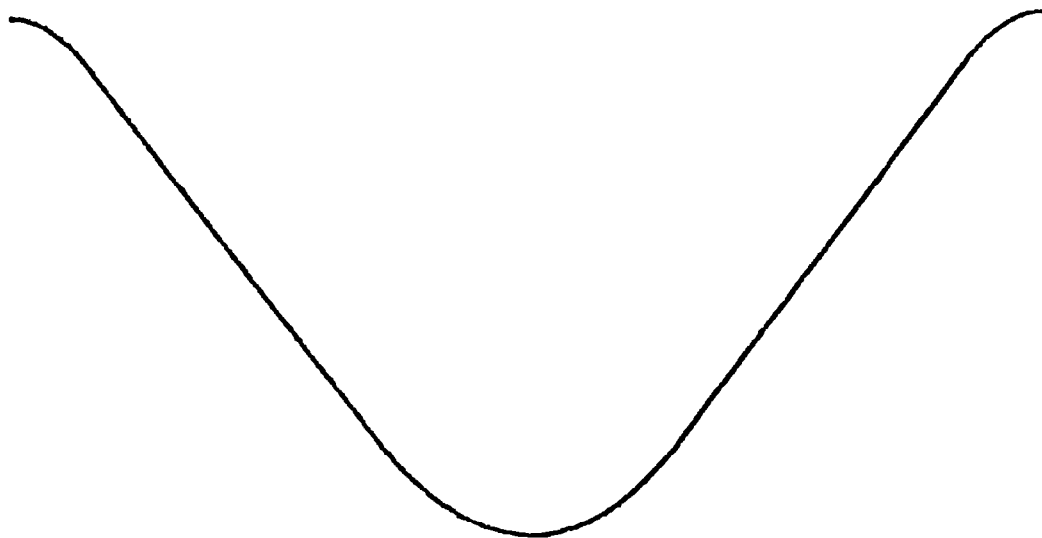
Time	3.6	4.2	4.8	5.4	6.0
$C_{D_f} \times 10^3$	3.663	3.624	3.587	3.552	3.519
$C_{D_p} \times 10^3$	0.534	0.492	0.476	0.470	0.468
$C_{D_T} \times 10^3$	4.198	4.117	4.063	4.022	3.986
% Drag Change	14.2	13.0	12.4	12.13	11.88



Entry B8

Surface shape same as B7 except that convex curvature is $\kappa = 1/\text{in.}$ and the concave curvature $\kappa = 0.5/\text{in.}$ ($a = 0.015"$ $\lambda = 1"$)

Time	3.6	4.2	4.8	5.4	6.0
$C_{D_f} \times 10^3$	3.662	3.622	3.584	3.549	3.515
$C_{D_p} \times 10^3$	0.564	0.521	0.504	0.497	0.494
$C_{D_T} \times 10^3$	4.226	4.143	4.088	4.046	4.009
% Drag Change	14.9	13.7	13.1	12.8	12.5



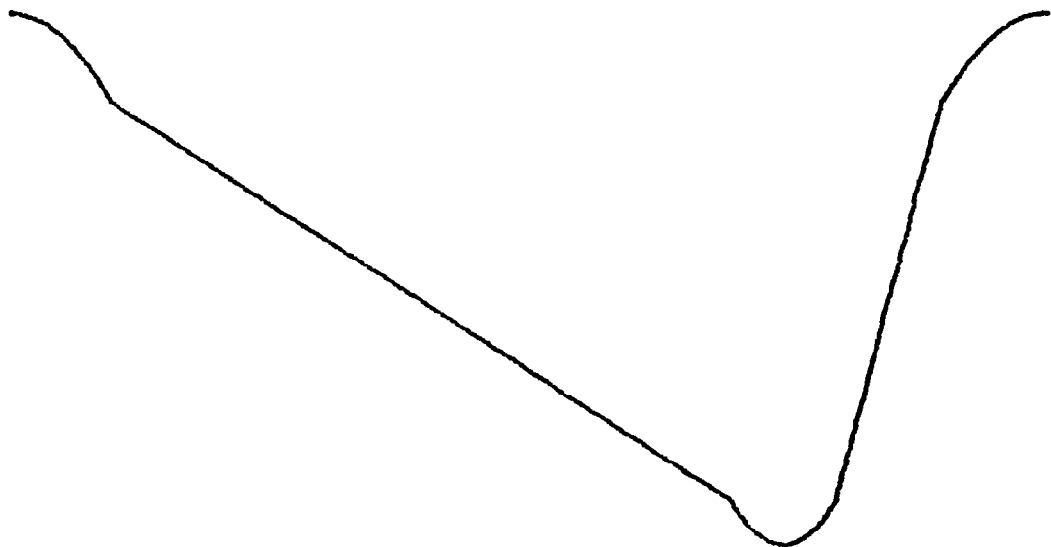
Entry B9

Unsymmetric Rounded shape.

This surface has a convex curvature (at the crests) $\kappa = 1/\text{in.}$ and concave curvature $\kappa = 0.5/\text{in.}$ Crest to trough distance in downwind direction is 0.75λ . The curvature extends to 0.1λ on either side of crest and trough followed by straight line segment ($\kappa = 0$). The extent of straight line segment is 0.6λ from crest to trough and 0.2λ from trough to crest.

Time	3.6	4.2	4.8	5.4	6.0
$C_{D_f} \times 10^3$	3.474	3.408	3.326	3.250	3.180
$C_{D_p} \times 10^3$	0.453	0.383	0.344	0.324	0.314
$C_{D_T} \times 10^3$	3.946	3.790	3.670	3.574	3.494
% Drag Change	7.37	4.03	1.55	-0.4	-2

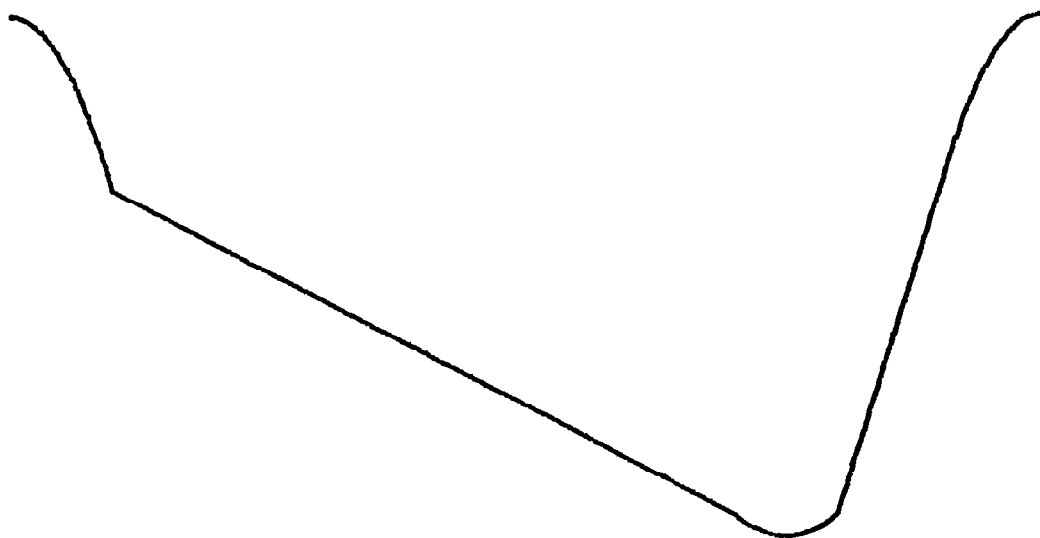
There is a possibility of drag reduction for this case!



Entry B10

The surface shape is similar to B9 except that the curvature on the crest side is now 0.5/in. and at the trough side is 1/in.

Time	3.6	4.2	4.8	5.4	6.0
$C_{D_f} \times 10^3$	3.517	3.439	3.365	3.297	3.233
$C_{D_p} \times 10^3$	0.465	0.395	0.357	0.335	0.323
$C_{D_T} \times 10^3$	3.982	3.834	3.722	3.632	3.556
% Drag Change	8.30	5.24	2.98	1.25	-0.2

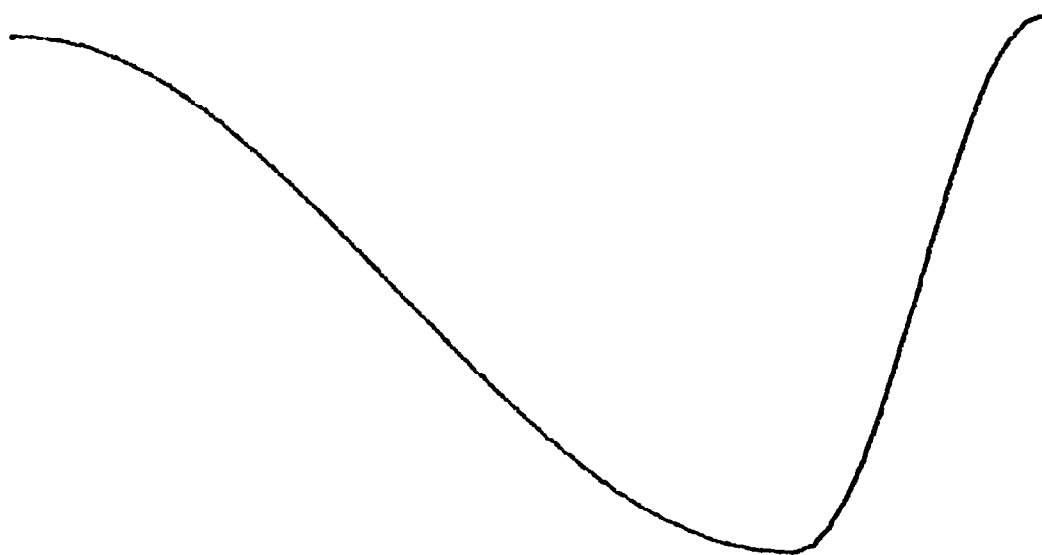


Entry B11 through B13 are sinusoidal surfaces that are asymmetric with $a = 0.015"$, $\lambda = 1"$

Entry B11

Surface $y \approx a \cos(k_1 x)$ $0 < x/\lambda < 0.75$ $k_1 = 2/3k$
 $y = a \cos(k_2 x)$ $0.75 < x/\lambda \leq 1.0$ $k_2 \approx 2k$.

Time	3.6	4.2	4.8	5.4	6.0
$C_{D_f} \times 10^3$	3.629	3.580	3.534	3.492	3.453
$C_{D_p} \times 10^3$	0.522	0.451	0.412	0.388	0.372
$C_{D_T} \times 10^3$	4.151	4.031	3.945	3.88	3.825
% Drag Change	13.0	10.7	9.16	8.17	7.35



Entry B12

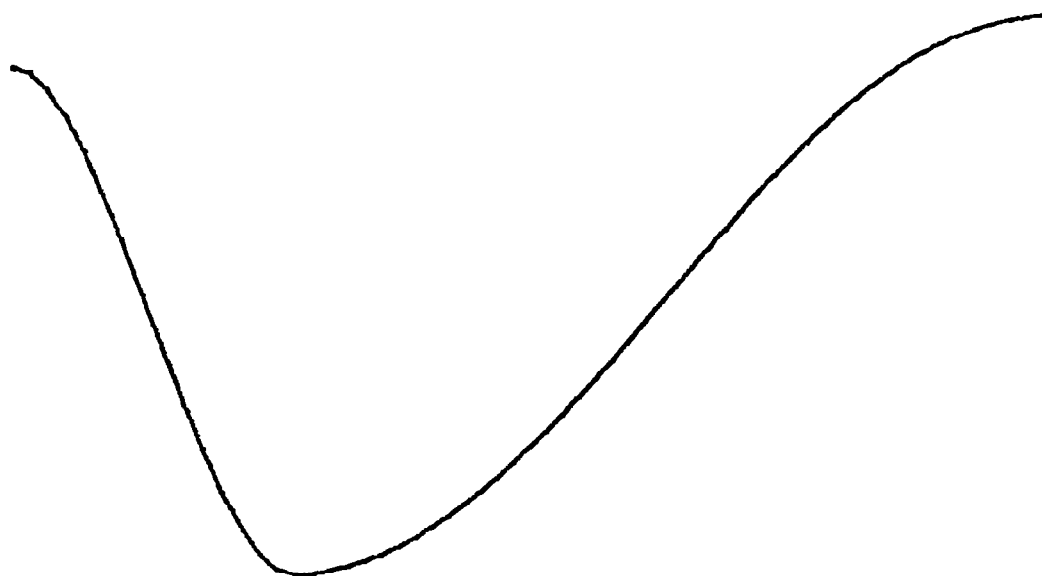
The surface shape is the same with the flow direction reversed.

i.e. $y = a \cos k_2 x$ $0 < x/\lambda < .75$

$y = a \cos k_1 (x - .25\lambda)$ $.75 < x/\lambda \leq 1.0$

Time	3.6	4.2	4.8	5.4	6.0
$C_{D_f} \times 10^3$	3.675	3.632	3.595	3.563	3.533
$C_{D_p} \times 10^3$	0.993	0.979	0.998	1.010	1.023
$C_{D_T} \times 10^3$	4.668	4.611	4.593	4.573	4.557
% Drag Change	27.1	26.6	27.1	27.5	27.8

Notice the drastic increase in total drag compared to B11.

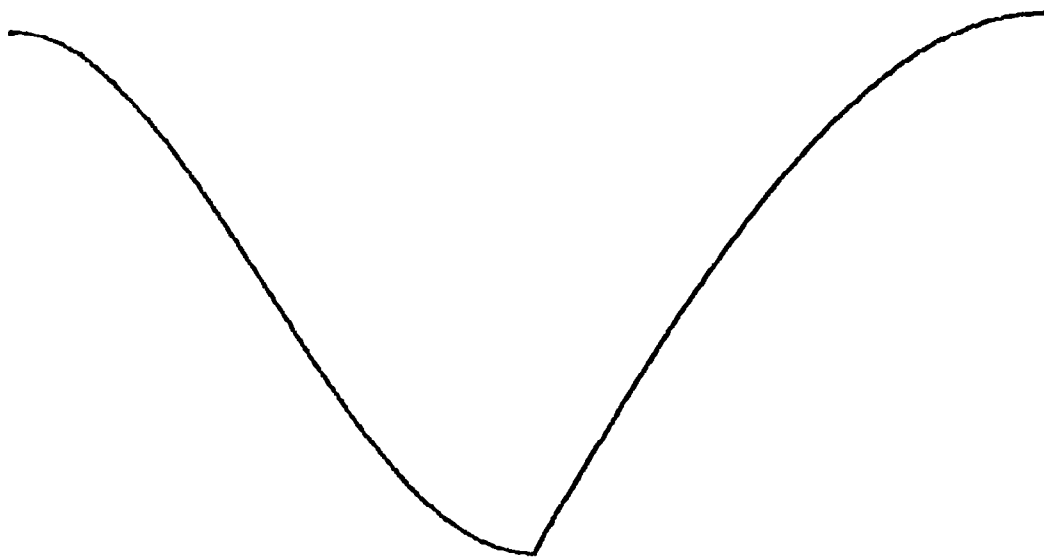


Entry B13

The surface can be described as

$$\begin{aligned} y &= a \cos kx & 0 < x/\lambda < 0.5 \\ y &= -a(1+2\cos kx/2)^{-1/2} & 0.5 \leq x/\lambda \leq 1.0 \end{aligned}$$

Time	3.6	4.2	4.8	5.4	6.0
$C_{D_f} \times 10^3$	3.642	3.598	3.557	3.518	3.482
$C_{D_p} \times 10^3$.542	0.503	0.490	0.487	0.487
$C_{D_T} \times 10^3$	4.184	4.101	4.047	4.005	3.969
% Drag Change	13.9	12.6	12.0	11.7	11.4



Entry B14 through B17 are hybrid sine straight line surfaces

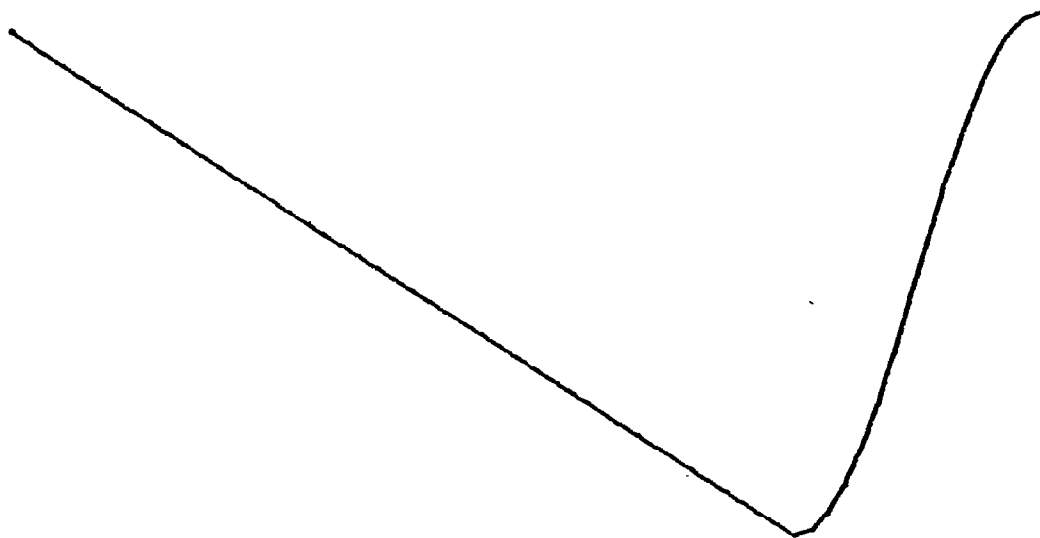
Entry B14

$$a = 0.015" \quad \lambda = 1"$$

$$y \approx a(1 - 2.66x/\lambda) \quad 0 < x/\lambda < 0.75$$

$$y = a \cos(4\pi(x-0.5)/\lambda) \quad 0.75 < x/\lambda < 1.0$$

Time	3.6	4.2	4.8	5.4	6.0
$C_{D_f} \times 10^3$			3.495	3.444	3.398
$C_{D_p} \times 10^3$			0.382	0.360	0.344
$C_{D_T} \times 10^3$			3.877	3.804	3.742
% Drag Change			7.28	6.05	5.0

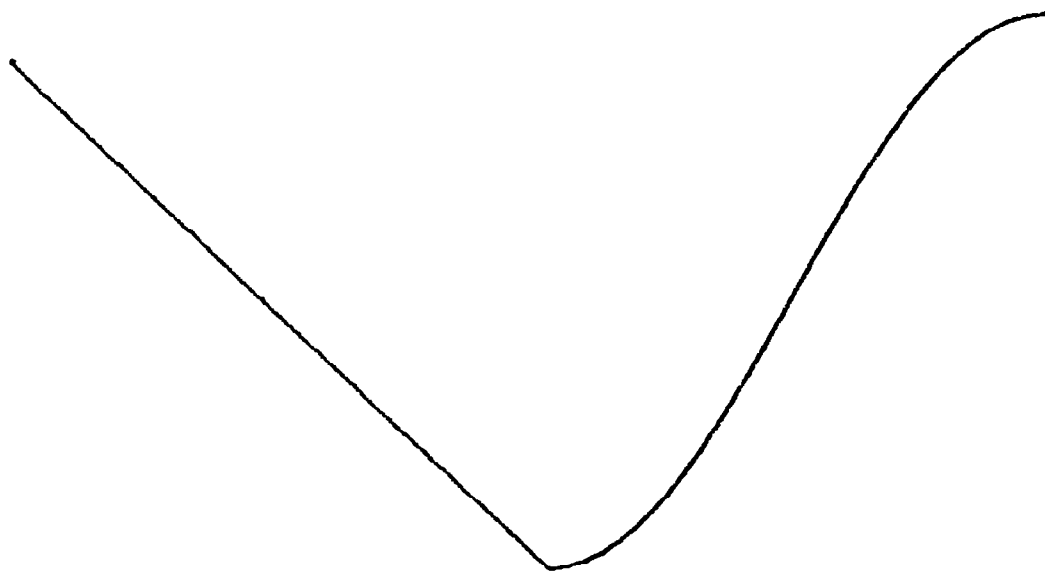


Entry B15

$$a = 0.015'' \quad \lambda = 1$$

Surface: $y \approx a (a - 4x/\lambda) \quad 0 < x/\lambda < 0.5$
 $y = a \cos 2\pi x/\lambda \quad 0.5 < x/\lambda < 1.0$

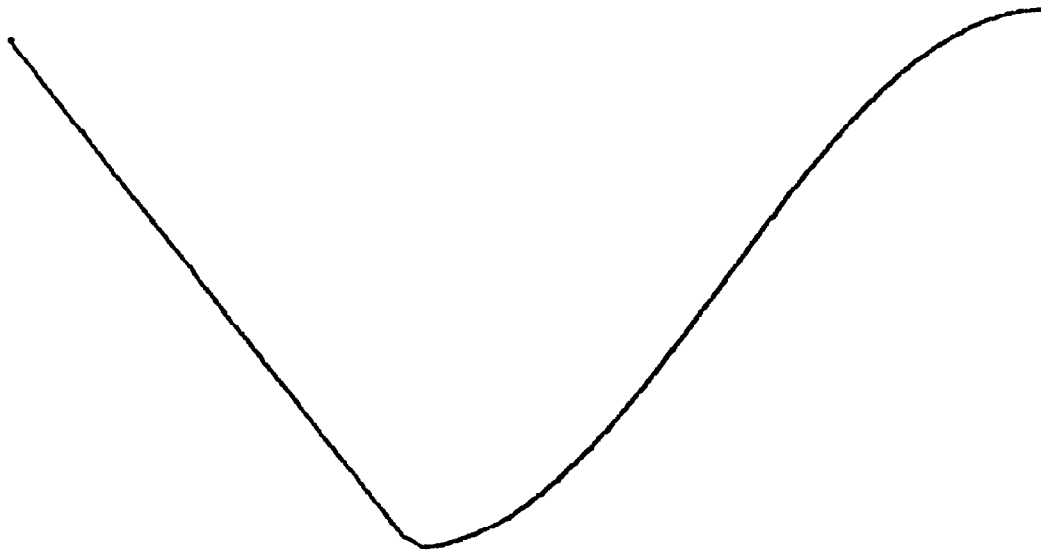
Time	3.6	4.2	4.8	5.4	6.0
$C_{D_f} \times 10^3$	3.667	3.628	3.591	3.557	3.524
$C_{D_p} \times 10^3$	0.484	0.442	0.424	0.414	0.408
$C_{D_T} \times 10^3$	4.151	4.070	4.015	3.971	3.932
% Drag Change	12.99	11.7	11.1	10.7	10.4



Entry B16

Surface: $y = a(1 - 5.33 x/\lambda)$ $0 < x/\lambda < 0.375$
 $y = a \cos[(x + .25\lambda)k_1]$ $0.375 < x/\lambda < k_0$
 where $k_1 \approx 1.6\pi/\lambda$

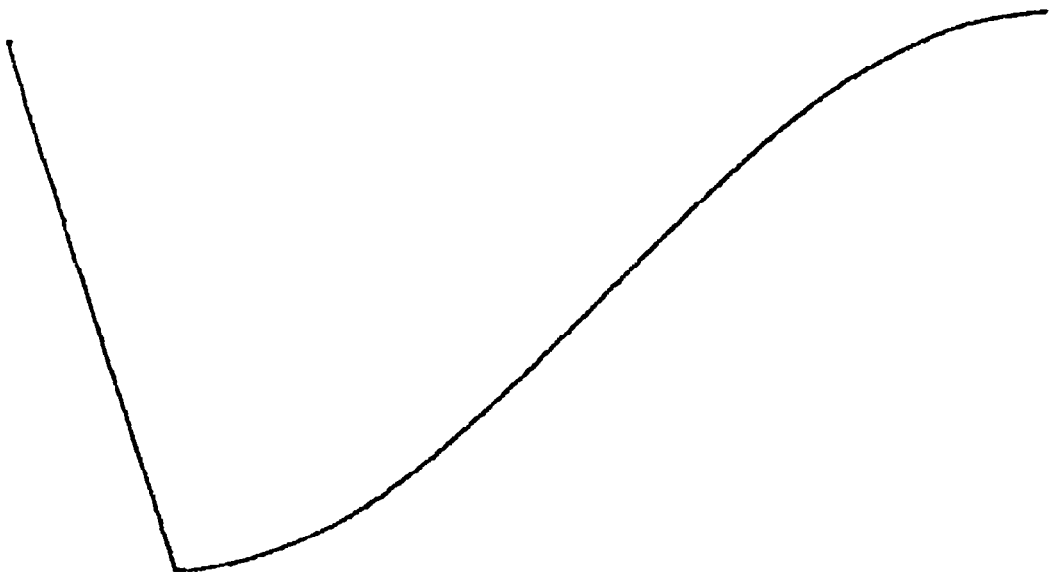
Time	3.6	4.2	4.8	5.4	6.0
$C_{D_f} \times 10^3$	3.676	3.638	3.602	3.568	3.536
$C_{D_p} \times 10^3$	0.554	0.518	0.504	0.500	0.500
$C_{D_T} \times 10^3$	4.230	4.156	4.106	4.068	4.036
% Drag Change	15.1	14.1	13.6	13.4	13.3



Entry B17

where $y = a(1 - 13.3x/\lambda)$ $0 < x/\lambda < 0.15$
 $y = a \cos (x + 0.70\lambda) k_1$ $0.15 < x/\lambda < 1.0$
 $k_1 \approx (1.176\pi/\lambda)$

Time	3.6	4.2	4.8	5.4	6.0
$C_{D_f} \times 10^3$	3.878	3.898	3.917	3.93	3.940
$C_{D_p} \times 10^3$	1.048	1.036	1.051	1.08	1.145
$C_{D_T} \times 10^3$	4.927	4.934	4.967	5.011	5.054
% Drag Change	34.1	35.4	37.4	39.7	41.8

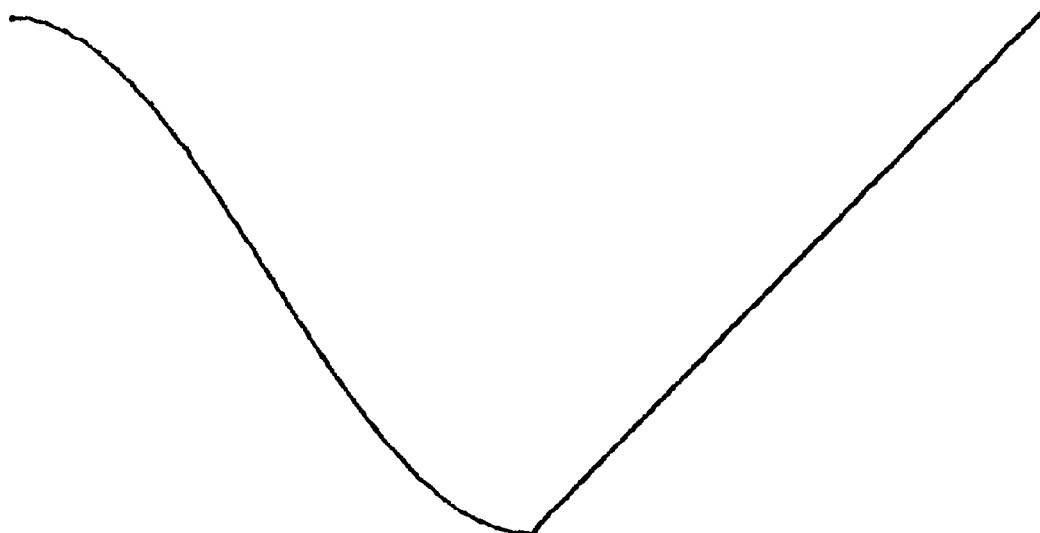


Entry B18

Surface: $y = a \cos 2\pi x/\lambda$ $0 < x/\lambda < 0.5$
 $y = a(4x/\lambda - 3)$ $0.5 < x/\lambda < 1.0$

Time	3.6	4.2	4.8	5.4	6.0
$C_{D_f} \times 10^3$	3.654	3.612	3.572	3.535	3.499
$C_{D_p} \times 10^3$	0.542	0.508	0.496	0.495	0.496
$C_{D_T} \times 10^3$	4.195	4.120	4.096	4.030	3.995
% Drag Change	14.18	13.1	12.6	12.4	12.1

Notice the slightly larger pressure drag for this case compared to B15 where the flow encounters the straight segment first and the sinusoidal region later.



Secondary Instability of Wall Bounded Shear Flows

The process by which a laminar shear flow undergoes transition to turbulence is of major interest in fluid dynamics. Here we study the initial transitional process that leads to eventual breakdown of wall bounded shear flows .

The process by which a laminar flow may become turbulent, i.e., the transition process, depends greatly on the geometry, initial conditions and other specific features of the flow. For flows like Benard Convection and Taylor couette flow a sequence of ordered states of transition may be discerned. With increasing Reynolds numbers, chaos results in these flows through either (i) infinitely many period-doubling bifurcations; (ii) intermittent chaotic states; or (iii) three incommensurate Hopf bifurcations. The choice of which route the flow undertakes in the transition process seems to depend on the specific details of the flow, the geometry and initial conditions. This sensitivity is probably due to the comparatively low Re numbers at which weak chaos appear in these flows.

The situation in wall bounded shear flows is different. The transition to turbulence is violent in the sense that the flow snaps from a laminar state to a strongly chaotic state with no apparent intervening stable bifurcations from the mean flow.

The instability proces can be categorized into

- (i) Primary (linear instability) of the basic shear flow
- (ii) Nonlinear saturation of the primary instabilty and the eventual formation of the secondary flow.
- and (iii) the secondary instability i.e. linear instability of the secondary flow.

A rational analysis of the physics of the instability requires understanding the roles of each of these three stages in the growth of disturbances that leads to breakdown of flow. In this section a summary of the work in progress in the area of stage (iii) is presented.

For analysis the primary instability was chosen as two-dimensional. The two dimensional primary instability results in a periodic nonlinear flow whereas the secondary instability likely leads to chaos. The secondary instability is assumed three-dimensional. The choice of two dimensionality of the primary instability is assumed with the understanding that though calculations of three-dimensional primary instabilities show an eventual transition to a chaotic state, the time and space scale of these instabilities do not bear connection to experimental observations. On the other hand the secondary instability considered here are inherently three dimensional, and have explosive growth rates (convective) as against primary instability (which grows in diffusive time scales).

Method

To study nonlinear saturation of the primary two dimensional instability in plane poiseuille flow the velocity is written of the form

$$\vec{V}(2) = U_1(z) \times + \sum_{-N}^N \vec{V}_n(2)(z, \tau), e^{i\alpha n x}$$

The two dimensional velocity field may be specified as

$$\vec{V}(2) = U_1(z) \times + \sum_{-N}^N \vec{V}(2)(z, \tau) e^{i\alpha(x - ct)}$$

where the time scale t is for the propagation of the nonlinear waves and the time scale τ is related to the attenuation of the travelling waves i.e. $\tau = t/R$ (τ is the diffusive time scale). The presence of the slow time scale in the evolution of general nonlinear two dimensional disturbances can be studied by perturbing the equilibria that are independent of τ . In plane Poiseuille flow there are stable quasi-equilibrium states at sufficiently low Reynolds numbers i.e., $R < 2900$ and equilibrium states between $2900 < R < 5000$ suggesting the role of the slow time scale in this problem. On the other hand axisymmetric pipe flow is stable to all finite amplitude perturbations. Our calculations suggest that for pipe flows the diffusive scale τ does not play a role in the evolution of axisymmetric perturbation of the pipe flow.

Results for Plane Poiseuille Flow

The flows to be studied are assumed to be of the form of a general two dimensional velocity for which an infinite small three dimensional disturbance is superposed.

i.e.,

$$\vec{V} = U_{||}(z) \hat{x} + \sum_{n=-N}^N \vec{V}_n^{(2)}(z,t) e^{i\alpha_n x} + \epsilon \vec{V}^{(3)}, \quad \epsilon \ll 1$$

$$\vec{V}^{(3)} = \sum_{m=\pm 1} \sum_{n=-N}^{+N} \vec{V}_{nm}^{(3)}(z,t) e^{i\beta_m y} e^{i\alpha_n x}$$

i.e., the choice is of only one mode in the spanwise direction (due to linear separability). N modes are kept in the stream direction due to nonlinear effects.

Using the multiple (2 time) scales we write

$$\vec{V} = U_1(z) x + \sum_{n=-N}^N \vec{V}_n(2)(z, \tau) e^{i\alpha_n(x-ct)} + \\ \epsilon \{ e^{\sigma t} \sum_{m=\pm 1}^N \sum_{n=-N}^N \vec{V}_{nm}(3)(z, \tau) e^{i\beta_m y} e^{i\alpha_n(x-ct)} \}$$

Thus σ is the growth rate of then three dimensional secondary instability.

The results of our calculations are briefly summarized a follows for plane Poiseuille flow. For $Re = 2900$, for β greater than a threshold value ($\beta \approx \alpha$ for maximum growth) the three dimensional perturbation grows in a time scale ($\sigma \approx 0(1)$).

For analysis of the secondary instability mechanisms at lower Reynolds numbers, a primary mode at a high Reynolds number is chosen (e.g. $R = 4000$). It is seen that the three dimensional disturbances turn off below $R < 400$: as $R \rightarrow \infty$ the growth rate is independant of R and hence the instability is inviscid in nature. In particular for $R \approx 1000$ or less, viscosity significantly limits the growth rate.

Secondary Instabilities of Free Shear Flows

The mechanism of secondary instability of free shear flows was investigated using the techniques discussed in the last section. The results for incompressible flows indicate that the secondary instabilities are convective in character, with a convective growth rate of 0.2. This is in agreement with Nishioka's experiments. The effect of compressibility on the secondary instabilities is also under current investigation. Work is also under progress on the Cyber 203 on compressible turbulent boundary layers.

Black Box Version of Compressible Sally Code

In recent years there has been attempts to design laminar flow control vehicles as a means of reducing fuel consumption of CTOL aircraft. The LFC technology has prompted renewed interest in the study of transition of both compressible and incompressible laminar boundary layers. The SALLY code was expressly developed as a design tool to perform efficient design calculations (eigen value calculations) of the stability of laminar boundary layers. The original version of the Sally code analyzes incompressible flows where the eigenvalue problem is the fourth order Orr-Sommerfeld equation system. For compressible boundary layers the eigen value problem is eighth order for a general three dimensional boundary layer. When the flow is two dimensional or in the absence of dissipation the eight order system reduces to sixth order.

The basic equations for the linear stability analysis of parallel flow compressible boundary layers are derived using the small disturbance theory. A set of five O.D.E.'s are obtained under the assumption of locally parallel flow (i.e. 3 second order momentum equations, 1 second order energy equation, and one first order continuity equations). This system of equations can be

reduced to a set of eight first order equations making the system amenable to an initial value numerical integration.

However, previous work in this area (i.e., initial value approach) suffers mainly in that often they are computationally slow and they require a reasonably good initial guess. Thus, they are not attractive as a design tool.

In the present work the original system of five equations are solved using finite difference matrix methods. The norm momentum equation is not converted to a first order equation for pressure since this generates unstable spurious modes when the problem is done using a global method.

Two eigenvalue search procedures are provided - (i) Global, when no initial guesses are available (ii) local, when a reasonable guess is available and refinements are required.

In the global approach care has to be taken to avoid the generation of spurious growing unstable modes that are physically not relevant. The spurious modes can be distinguished by refining the spatial discretisation; the number of true modes increase while the spurious modes remain the same.

A key concept that was used to eliminate the generation of spurious results in this work is that one can eliminate the spurious mode by using a numerical method for the stability problem that gives numerical stability for the initial value problem also. In this situation no spurious modes appear. Details of this work are reported in Ref. (17).

List of References

1. Balasubramanian, R. and Orszag, S. A.: "Drag Reduction Effects in Turbulent Boundary Layers Over Wavy Walls", NASA CR-159305, 1980.
2. Balasubramanian, R. and Orszag, S. A.: "Numerical Studies of Laminar and Turbulent Drag Reduction", NASA CR-3498, 1981.
3. Benjamin, T. B.: "Shearing Flow Over a Wavy Boundary", J. Fluid Mech. 6, 161; 1959.
4. Lamb, H., Hydrodynamics, 6th Edition, Cambridge University Press, Chapter IX, 1932.
5. Miles, J. W.: "On the Generation of Surface Waves by Shear Flows", J. Fluid Mech, 3, 185; 1957.
6. Kendall, J. M.: "The Turbulent Boundary Layer Over a Wall With Progressive Surface Waves". J. Fluid Mech., 41, 259; 1970; see Fig. 5, pp. 269.
7. Davis, R. E.: "On the Prediction of Turbulent Flow Over a Wavy Boundary". J. Fluid Mech., vol. 42; 1970, pp. 721-731.
8. Zilker, D. P.; Cook, G. W.; and Hanratty, T. J.: "Influence of the Amplitude of a Solid Wavy Wall on a Turbulent Flow. Part 1. Non-separated Flows", J. Fluid Mech., vol. 82, pt1; 1977; pp. 29-51.
9. Taylor, P. A.; Gent P. R.; and Keen, J. M.: "Some Numerical Solutions for Turbulent Boundary Layer Flow above Fixed, Rough Wavy Surfaces", Geophys. J. R. Astro. Soc., 44, 177; 1976.
10. Chalikov, D. V.: "The Numerical Simulation of Wind Wave Interaction", J. Fluid Mech., 87, pt 3, 561; 1978.
11. Markatos, N. C. G.: "Heat, Mass and Momentum Transfer Across a Wavy Boundary", Computer Methods in Applied Mechanics and Engineering, 14, 323; 1978.
12. Caponi, E. A.; Fornberg, B.; Knight, D. D.; Mclean, J. W.; Saffman, P. G. and Yuen, H. C.: "Calculation of Laminar Viscous Flow Over a Moving Wavy Surface". Proc. of Ninth National Congress of Theoretical and Applied Mechanics; June, 1982.
13. Cary, A. M., Jr.; Weinstein, L. M.; and Bushnell, D. M.: "Drag Reduction Characteristics of Small Amplitude Rigid Surface Waves", Viscous Flow Drag Reduction, Progress in Astronautics and Aeronautics, 72, 144; 1980.

14. Sigal, A.: "An Experimental Investigation of the Turbulent Boundary Layer Over a Wavy Wall", Phd. Thesis, California Institute of Technology, 1971.
15. Bushnell, D. M. and Beckwith, I. E.: "Calculation of Nonequilibrium Hypersonic Turbulent Boundary Layers and Comparison with Experimental Data". AIAA Journal, vol. 8; 1970, pp. 1462-1469.
16. Bushnell, D. M.; Watson, R. D.; and Holley, B. B.: "Mach and Reynolds Number Effects on Turbulent Skin Friction Reduction by Injection". Journal of Spacecraft and Rockets, vol. 12, No. 8; 1975; ppg. 506-508.
17. Malik, M. R.: "Finite-Difference Solution of the Compressible Stability Eigenvalue Problem", NASA CR-3584; 1982.

TABLE 1.1

 $R_x = 100, x = 10, U_0 = .216, \lambda = 1$
 $(x/\lambda = 10)$

a/λ	Benjamin's Theory								Navier-Stokes Results			
	Sinusoidal Profile				Linear Velocity Profile							
	C_{p_0}	ϕ	C_{f_0}	θ	C_{p_0}	ϕ	C_{f_0}	θ	C_{p_0}	ϕ	C_{f_0}	θ
10^{-4}	5.298×10^{-6}	219.7	8.294×10^{-6}	99.7	6.67×10^{-6}	147.8°	2.087×10^{-5}	27.8	5.4×10^{-5}	+92.2°	3×10^{-5}	+2.8°
10^{-3}	5.298×10^{-5}	219.7	8.294×10^{-5}	99.7	6.67×10^{-5}	147.8°	2.087×10^{-4}	27.8	5.22×10^{-4}	+92°	3.02×10^{-4}	2.10°
10^{-2}	5.298×10^{-4}	219.7	8.294×10^{-4}	99.7	6.67×10^{-4}	147.8°	2.087×10^{-3}	27.8	5.2×10^{-3}	91.1°	3.02×10^{-3}	2.16°
2×10^{-2}	1.050×10^{-3}	219.7	1.659×10^{-3}	99.7	1.33×10^{-3}	147.8°	4.174×10^{-3}	27.8	1.07×10^{-2}	91°	6.2×10^{-3}	2°
5×10^{-2}	2.65×10^{-3}	219.7	4.15×10^{-3}	99.7	3.34×10^{-3}	147.8°	1.04×10^{-2}	27.8	2.4×10^{-2}	91°	1.28×10^{-2}	1.3°
10^{-1}	5.298×10^{-3}	219.7	8.29×10^{-3}	99.7	6.67×10^{-3}	147.8°	2.087×10^{-2}	27.8	4.15×10^{-2}	90°	4.8×10^{-2}	2°

Note: $y_w = a \sin kx$, is the surface.

$$C_p(x) = C_{p_0} \sin(kx + \phi)$$

 $C_f = C_{f_0} \sin(kx + \theta) + C_{f_m}$, where C_{f_m} is the wave average mean skin friction.

TABLE 1.2 $R_x = 10^3$, $x = 10$, $U_0 = 2.16$, $\lambda = 1$

a/λ	Benjamin's Theory						Navier-Stokes Results			
	Sinusoidal Profile			Linear Velocity Profile						
	C_{p_0}	ϕ	C_{f_0}	θ	C_{p_0}	ϕ	C_{f_0}	θ	C_{p_0}	ϕ
10^{-4}	2.43×10^{-5}	112.8	1.20×10^{-5}	-7.16°	2.01×10^{-5}	149.3	1.99×10^{-5}	29.3	3.456×10^{-5}	120°
10^{-3}	2.43×10^{-4}	112.8	1.20×10^{-4}	-7.16°	2.01×10^{-4}	149.3	1.99×10^{-4}	29.3	3.28×10^{-4}	120°
10^{-2}	2.43×10^{-3}	112.8	1.20×10^{-3}	-7.16°	2.01×10^{-3}	149.3	1.99×10^{-3}	29.3	3.27×10^{-3}	120°
2×10^{-2}	4.86×10^{-3}	112.8	2.4×10^{-3}	-7.16°	4.02×10^{-3}	149.3	3.98×10^{-3}	21.3	6.45×10^{-3}	122°
5×10^{-2}	1.22×10^{-2}	112.8	6.0×10^{-2}	-7.16°	1.01×10^{-2}	149.3	1.00×10^{-2}	21.3	1.58×10^{-2} *	125°
									1.45×10^{-2}	
									8.118×10^{-3}	21°

*At this wavelength pronounced nonlinear effects are present in the pressure distribution.

TABLE 1.3 Benjamin's Theory $R_x = 10^4$, $\alpha = 10$, $U_0 = 2.16$, $\lambda = 1$ "

Benjamin's Theory												Navier-Stokes Results				
a/λ	Sinusoidal Profile					Linear Velocity Profile										
	C _{p₀}	φ	C _{f₀}	θ	C _{p₀}	φ	C _{f₀}	θ	C _{p₀}	φ	C _{f₀}	θ	C _{p₀}	φ	C _{f₀}	θ
10 ⁻⁴	6.25 x 10 ⁻³	136°	8.99 x 10 ⁻⁶	15.9°	6.25 x 10 ⁻³	150°	1.96 x 10 ⁻³	29.8	6.0 x 10 ⁻³	140°	1.224 x 10 ⁻³	30°				
10 ⁻³	6.25 x 10 ⁻⁴	136°	8.99 x 10 ⁻⁵	15.9°	6.26 x 10 ⁻⁴	150°	1.96 x 10 ⁻⁴	29.8	6.0 x 10 ⁻⁴	142°	1.598 x 10 ⁻⁴	30°				
10 ⁻²	6.25 x 10 ⁻³	136°	8.99 x 10 ⁻⁴	15.9°	6.26 x 10 ⁻³	150°	1.96 x 10 ⁻³	29.8	6.0 x 10 ⁻³	142°	1.581 x 10 ⁻³	31°				
2 x 10 ⁻²	1.25 x 10 ⁻²	136°	1.80 x 10 ⁻³	15.9°	1.25 x 10 ⁻²	150°	3.92 x 10 ⁻³	29.8	1.01 x 10 ⁻²	128° 142°	3.8 x 10 ⁻³	31°				
5 x 10 ⁻²	3.12 x 10 ⁻²	136°	4.40 x 10 ⁻³	15.9°	3.13 x 10 ⁻²	150°	9.8 x 10 ⁻³	29.8	2.58 x 10 ⁻²	114°	7.08 x 10 ⁻³	30°				
									2.014 x 10 ⁻²	155°		11°				

*At this waveheight pronounced nonlinear effects are present in the pressure distribution.

**Both the pressure and shear stress distributions are skewed because of large amplitude effects.

TABLE 1.4 $P_x = 10^4$, $\nu = 10^2$, $x = 10^2$, $\delta = 4.73$, $a/\lambda = 10^{-3}$

The Effect of Varying δ/λ on the Pressure Distributions

Benjamin's Theory				Navier-Stokes Results		
Sine Profile		Linear Profile		Blasius Profile		Linear Profile**
δ/λ	C_{p_0}	ϕ	C_{f_0}	ϕ	C_{p_0}	C_{f_0}
1.0	2.44×10^{-4}	128°	2.3×10^{-4}	150°	2.72×10^{-4}	2.57×10^{-4}
2.0	1.07×10^{-4}	119°	9.1×10^{-5}	150°	1.46×10^{-4}	1.32×10^{-4}
4.0	4.74×10^{-5}	100°	3.6×10^{-5}	150°	9.2×10^{-5}	8.2×10^{-5}
						ϕ
						135°
						125°
						110°

** Linear profile with same $U'(0)$ as Blasius profile was used in the calculations.

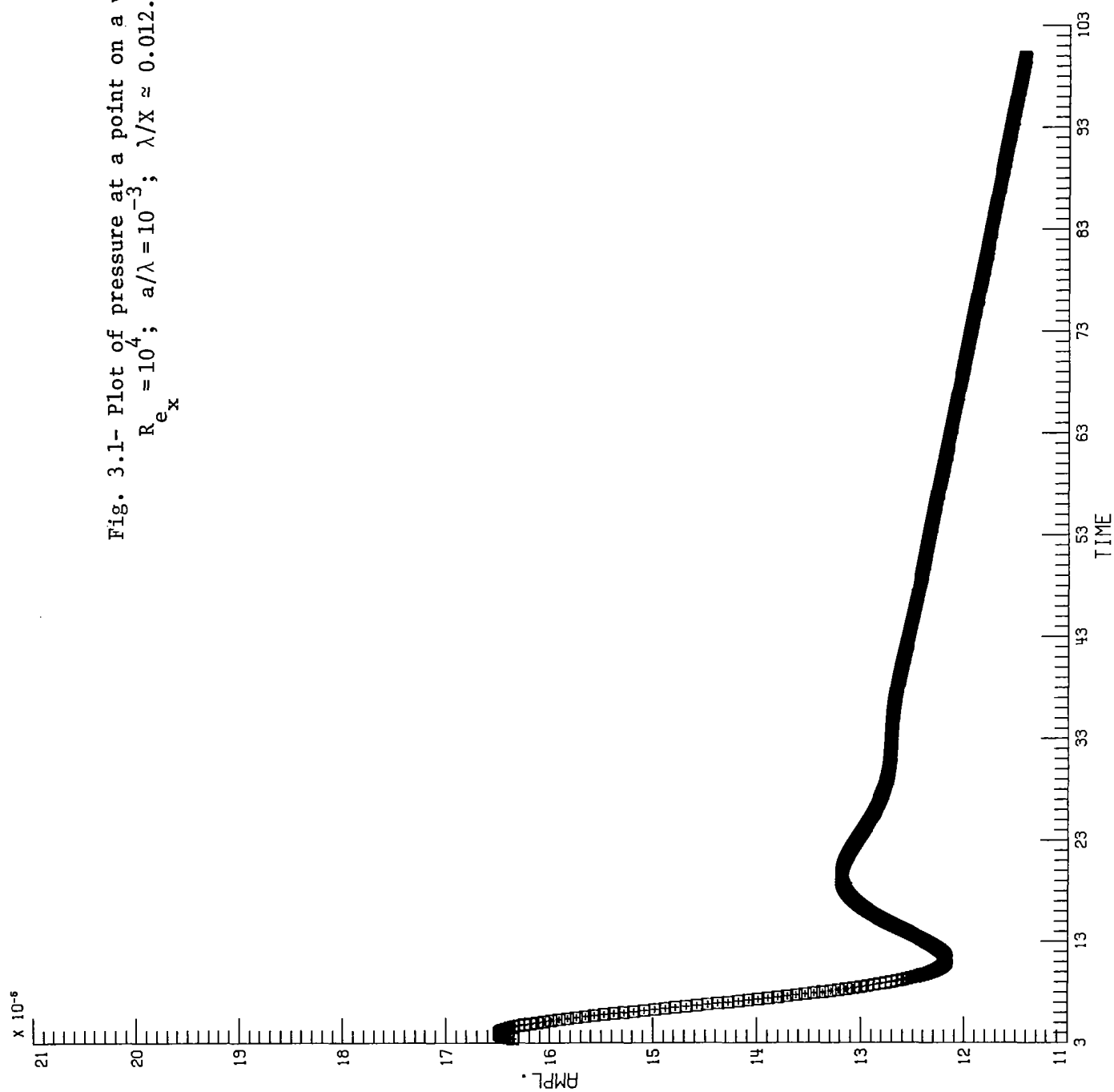
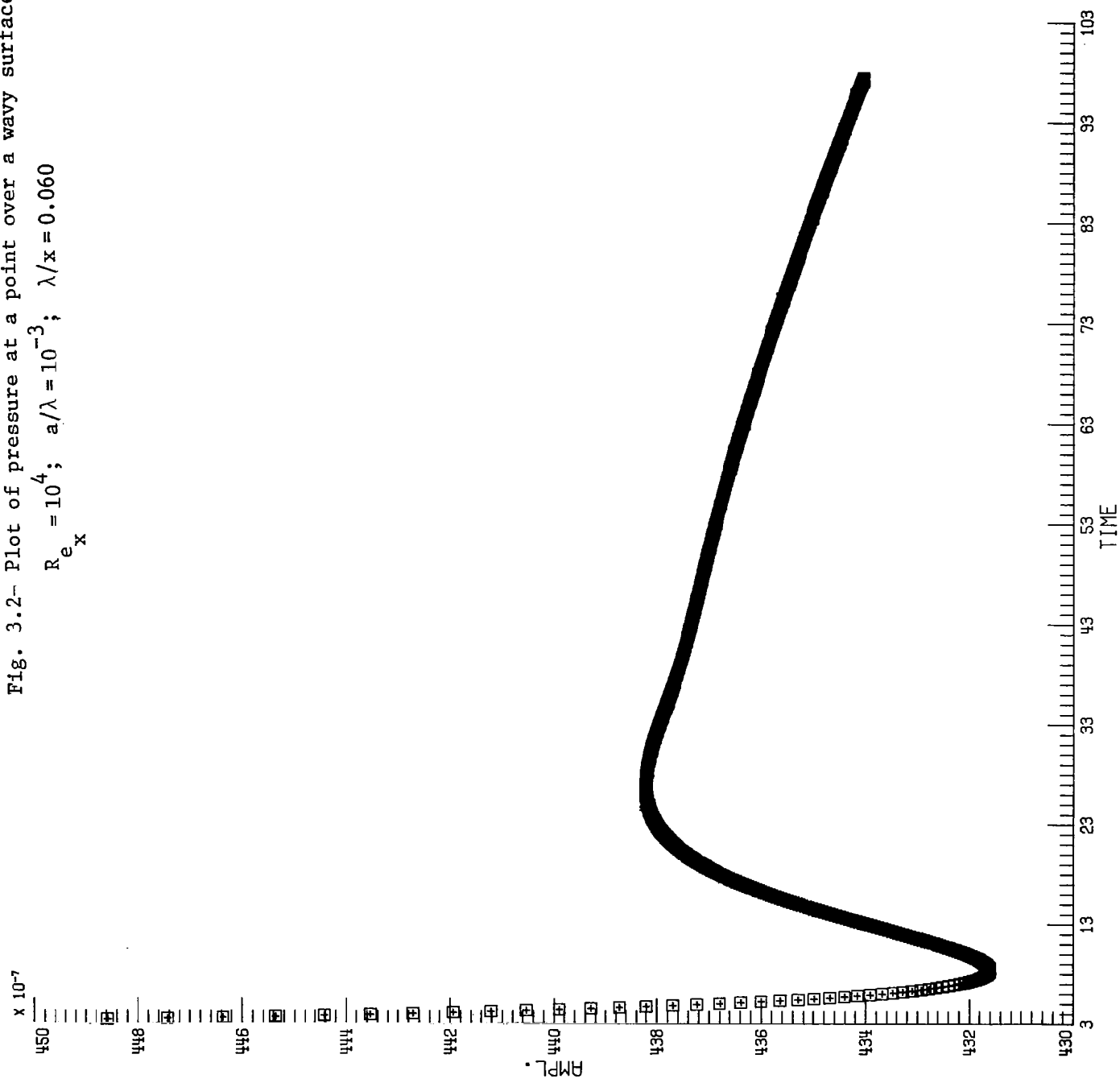


Fig. 3.1- Plot of pressure at a point on a wavy surface.
 $R_{ex} = 10^4$; $a/\lambda = 10^{-3}$; $\lambda/X \approx 0.012$.

Fig. 3.2- Plot of pressure at a point over a wavy surface vs time.
 $R_e = 10^4$; $a/\lambda = 10^{-3}$; $\lambda/x = 0.060$



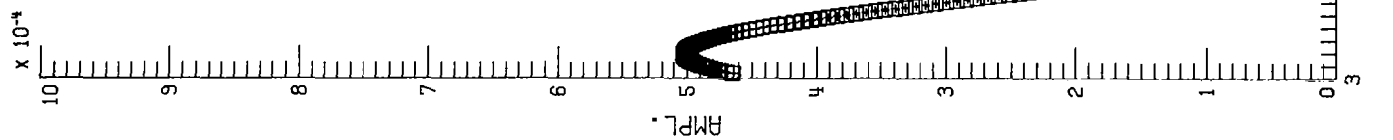
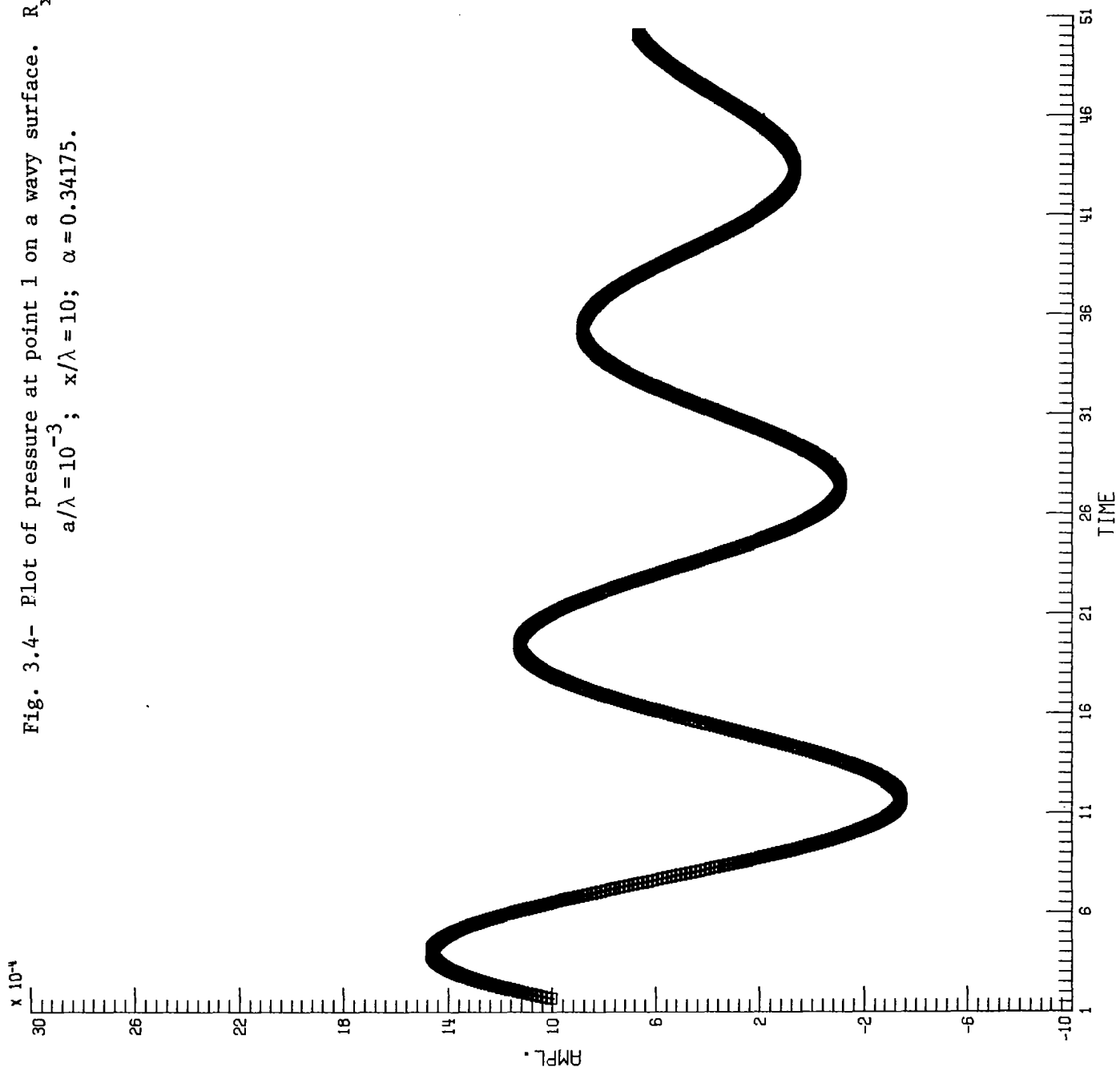


Fig. 3.3- Plot of pressure at a point over a wavy surface vs time. $R_e = 10^5$
 $a/\lambda = 2.5 \times 10^{-4}$; $x/\lambda = 5$; $\alpha = 0.1709$.

Fig. 3.4- Plot of pressure at point 1 on a wavy surface. $R_x = 10^5$
 $a/\lambda = 10^{-3}$; $x/\lambda = 10$; $\alpha = 0.34175$.



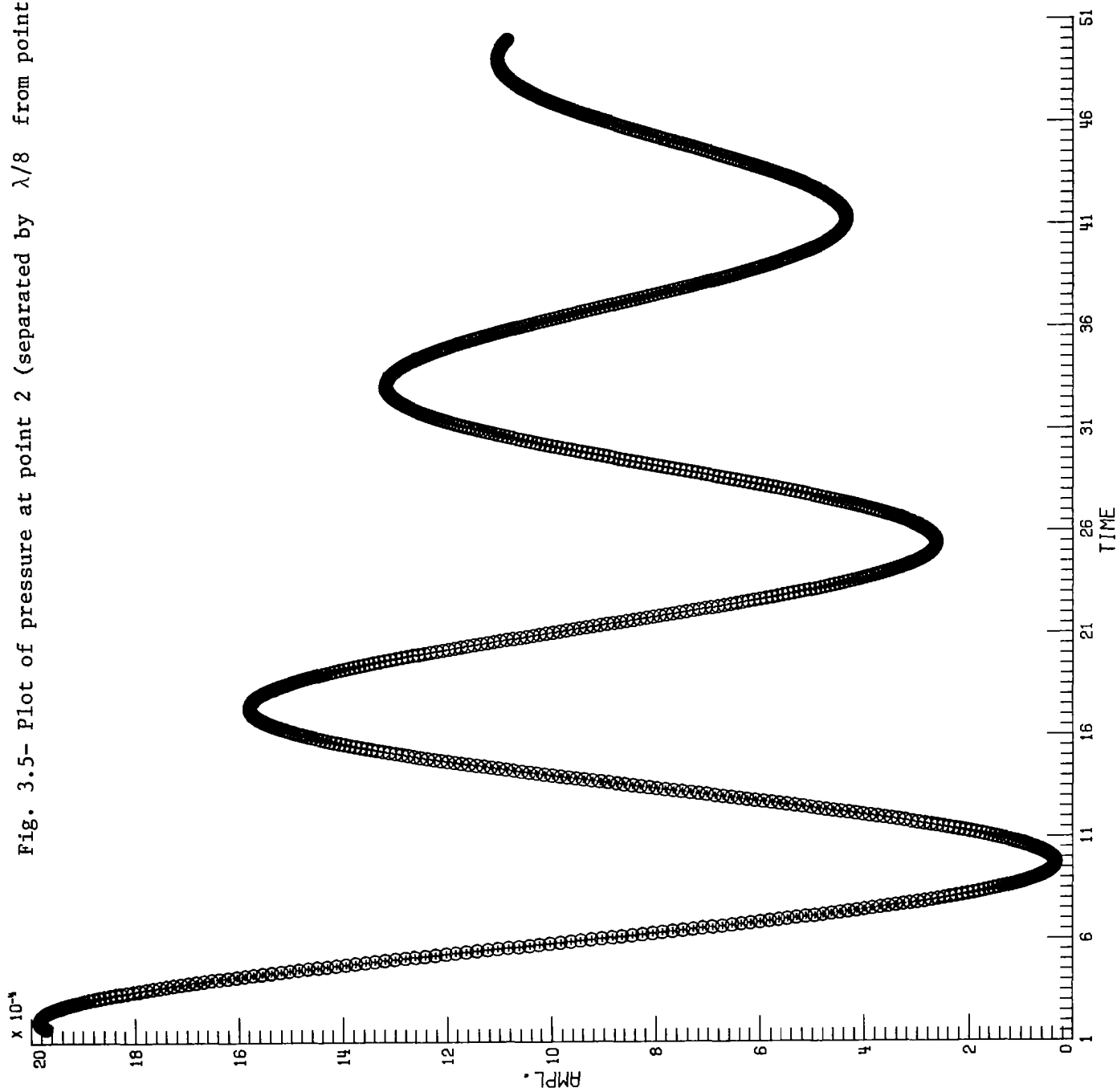


Fig. 3.5- Plot of pressure at point 2 (separated by $\lambda/8$ from point 1) vs time.

INFOPLT 2.

Fig. 3.6- Plot of pressure vs time for a wavy surface. $R_x = 10^5$;
 $a/\lambda = 5 \times 10^{-3}$; $\alpha = 0.34175$; $x/\lambda = 10$.

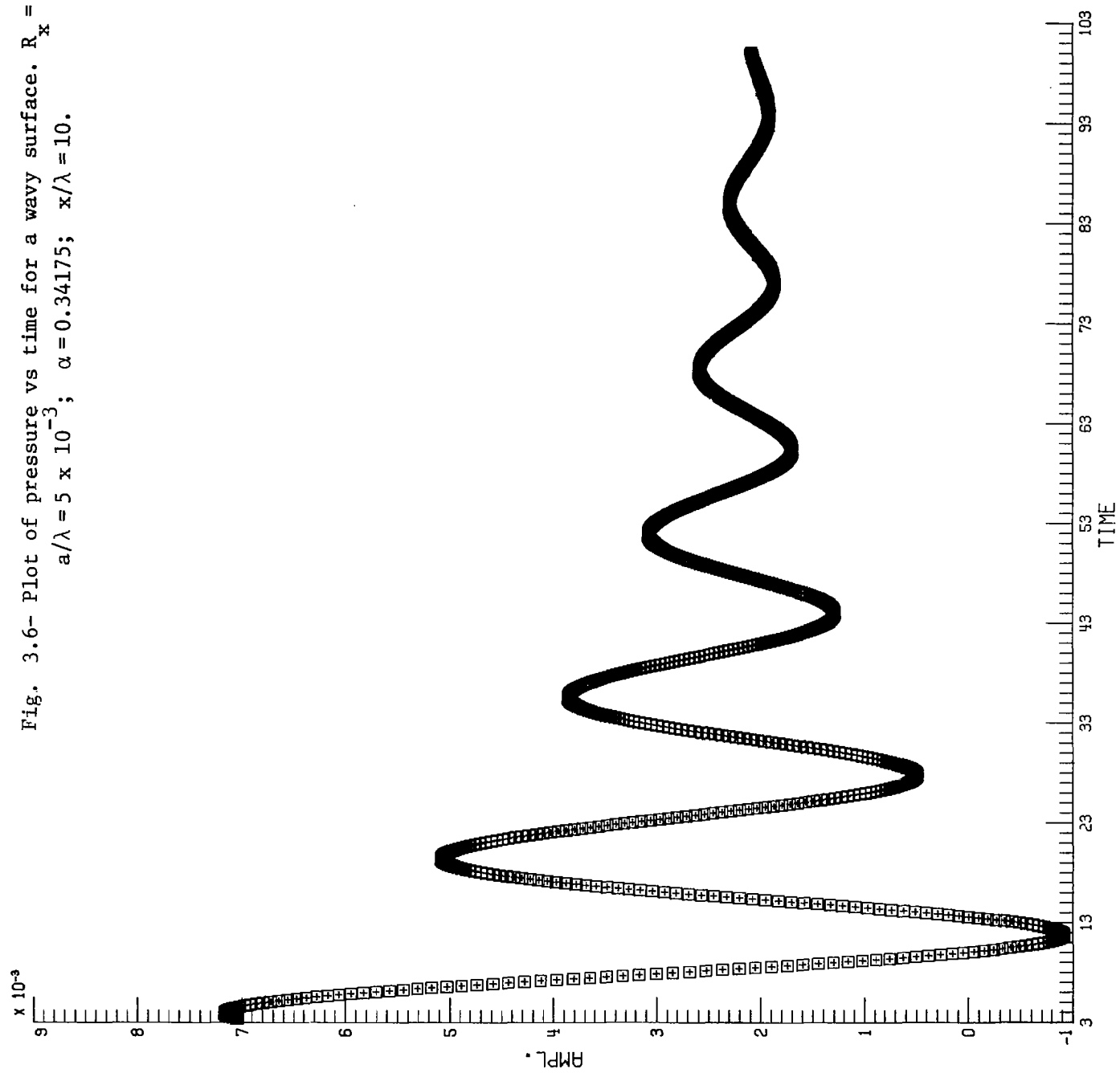


Fig. 3.7- Plot of pressure vs time at a point for a wavy surface.
 $R_x = 10^5$; $a/\lambda = 10^{-2}$; $\alpha = 0.34175$; $x/\lambda = 10$.

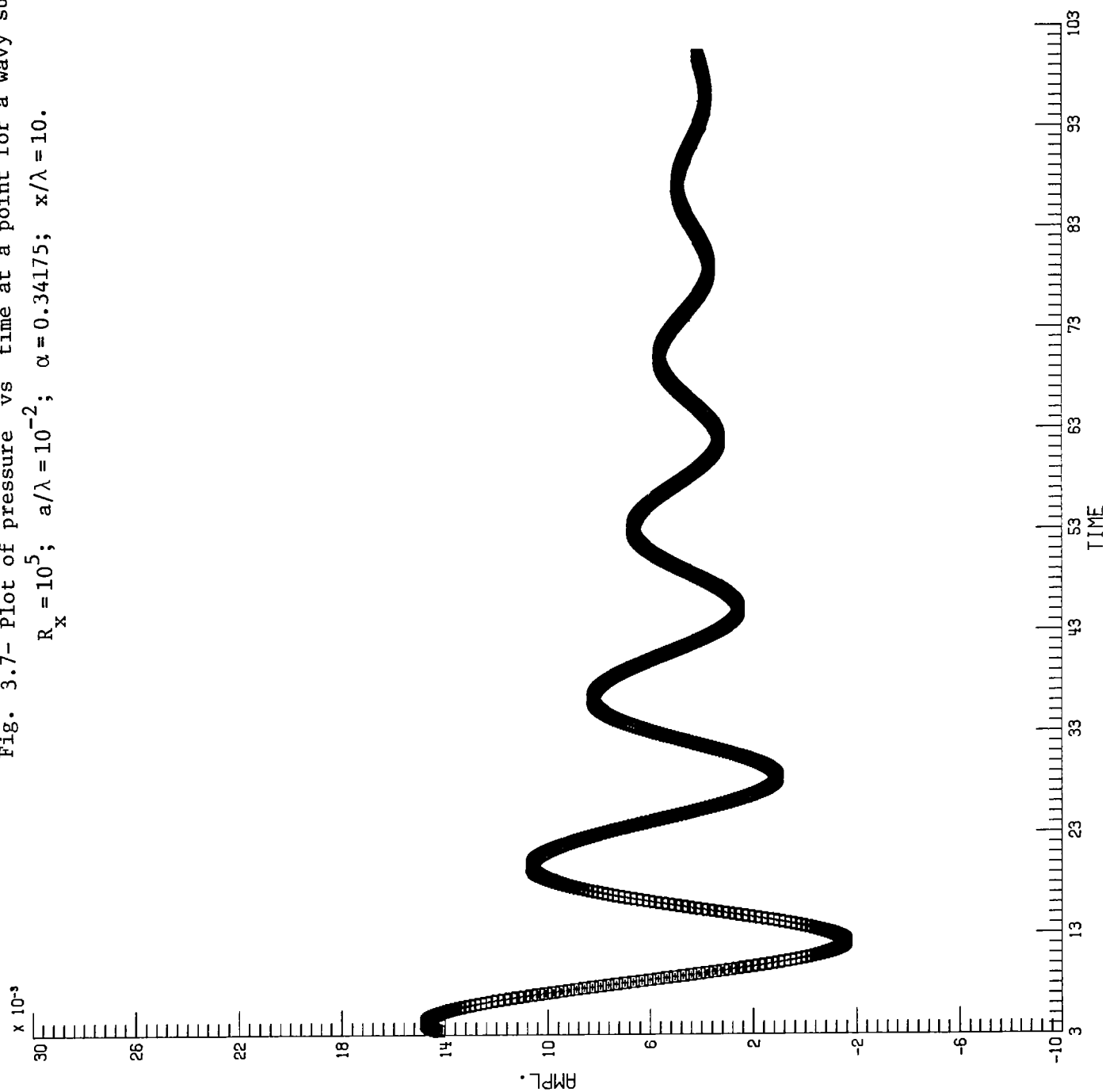


Fig. 3.8- Plot of pressure vs time at a point for a wavy surface.
 $R_x = 10^5$; $a/\lambda = 3 \times 10^{-2}$; $\alpha = 0.34175$; $x/\lambda = 10$.
 Flow separation occurs for this case.

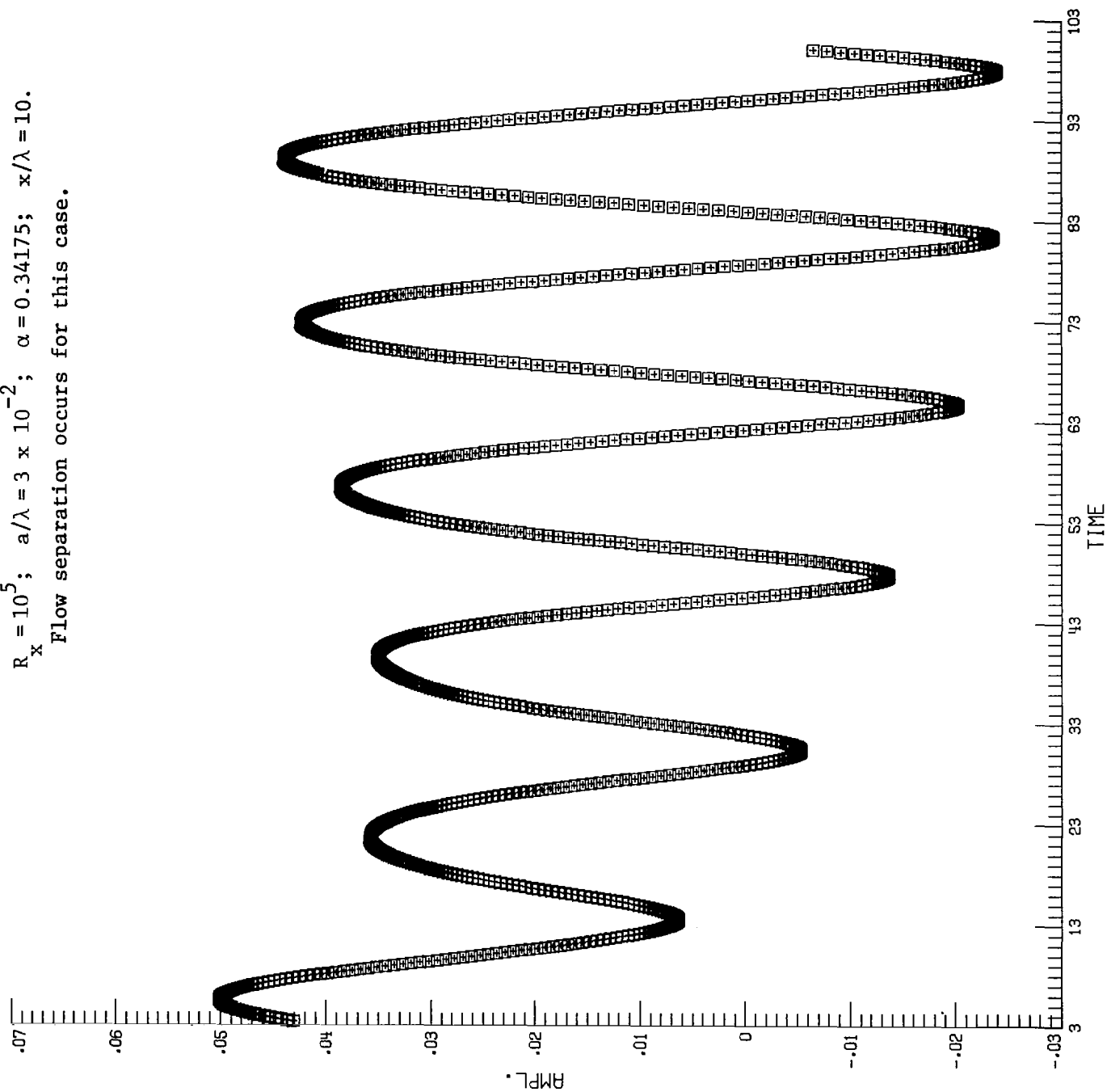


Fig. 3.9- Plot of pressure vs time at a point on a wavy surface.
 $R_x = 10^5$; $a/\lambda = 5 \times 10^{-2}$; $\alpha = 0.34175$; $x/\lambda = 10$.

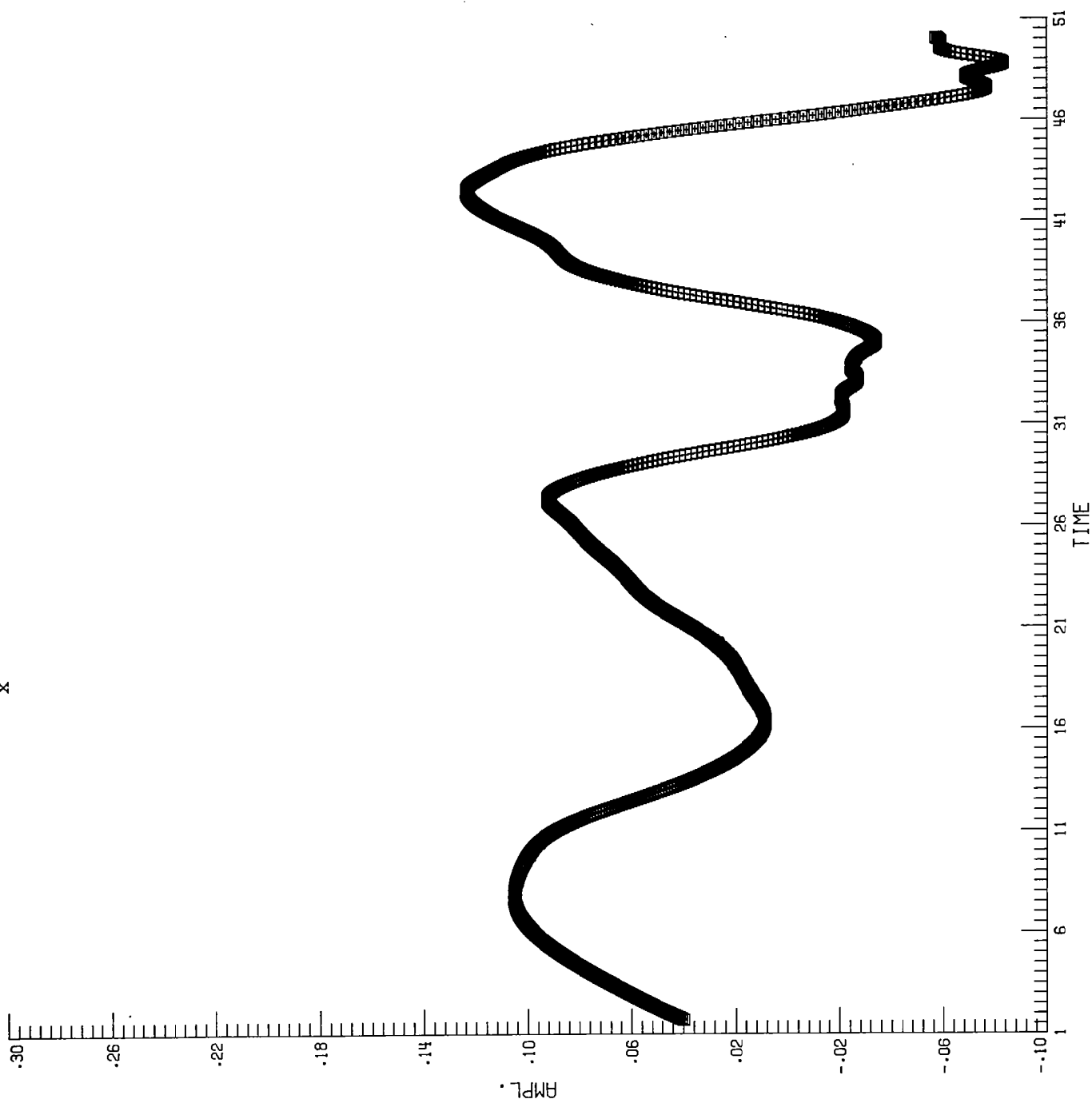
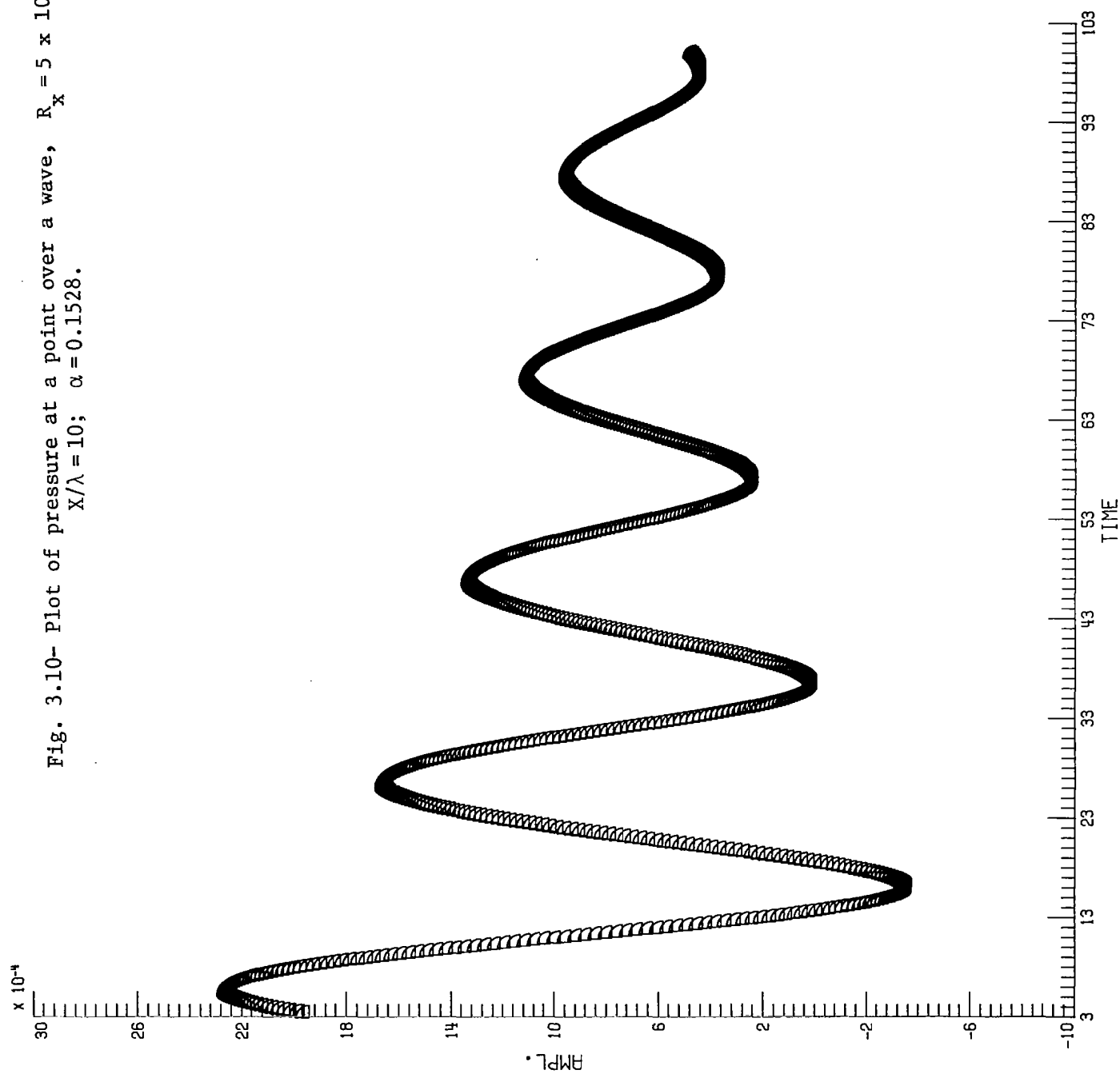


Fig. 3.10- Plot of pressure at a point over a wave, $R_x = 5 \times 10^5$; $a/\lambda = 10^{-3}$;
 $X/\lambda = 10$; $\alpha = 0.1528$.



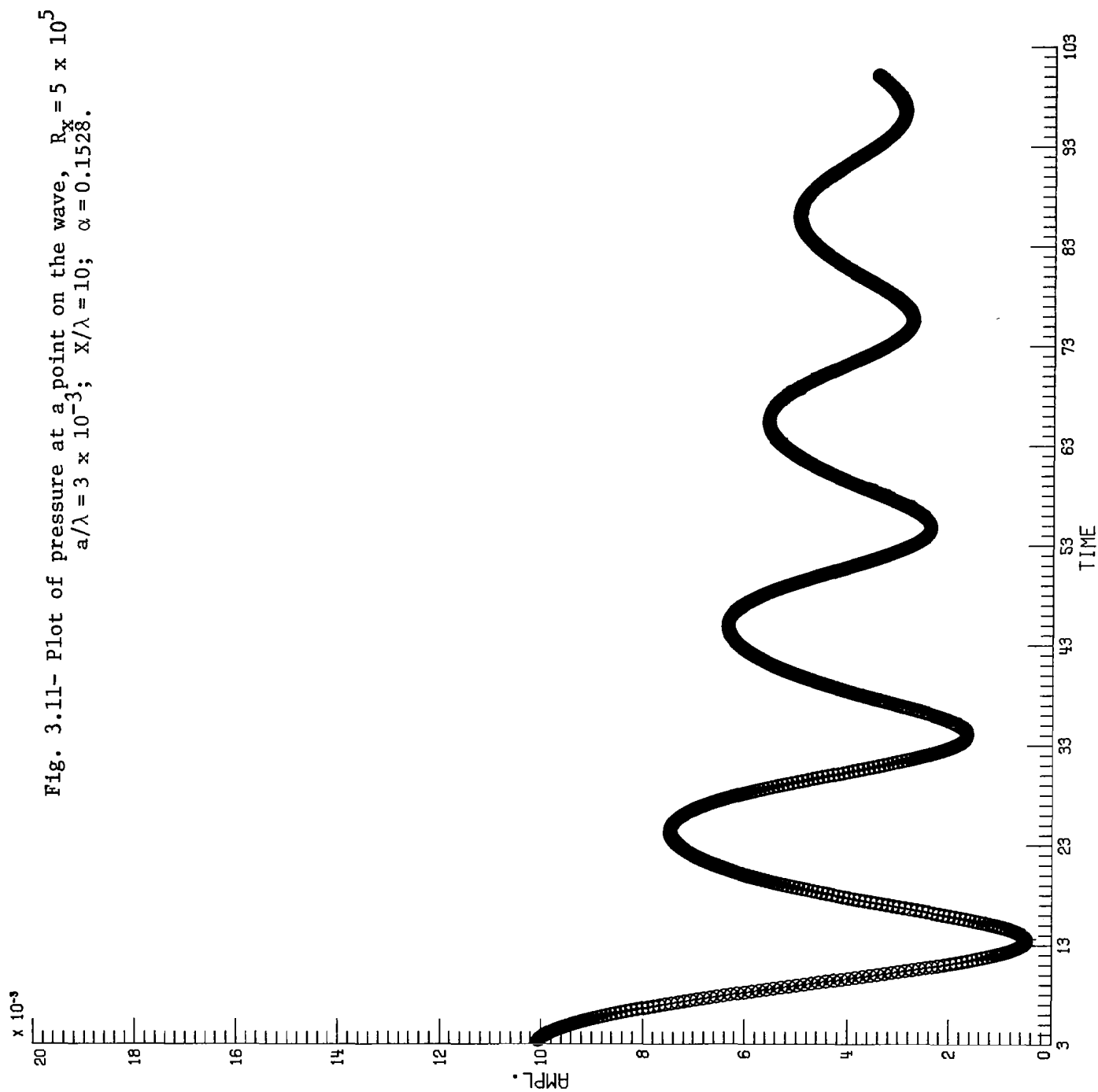


Fig. 3.12- Plot of pressure at point 1, $R_x = -5 \times 10^5$; $a/\lambda = 2 \times 10^{-2}$;
 $X/\lambda = 10$; $\alpha = 0.1528$.

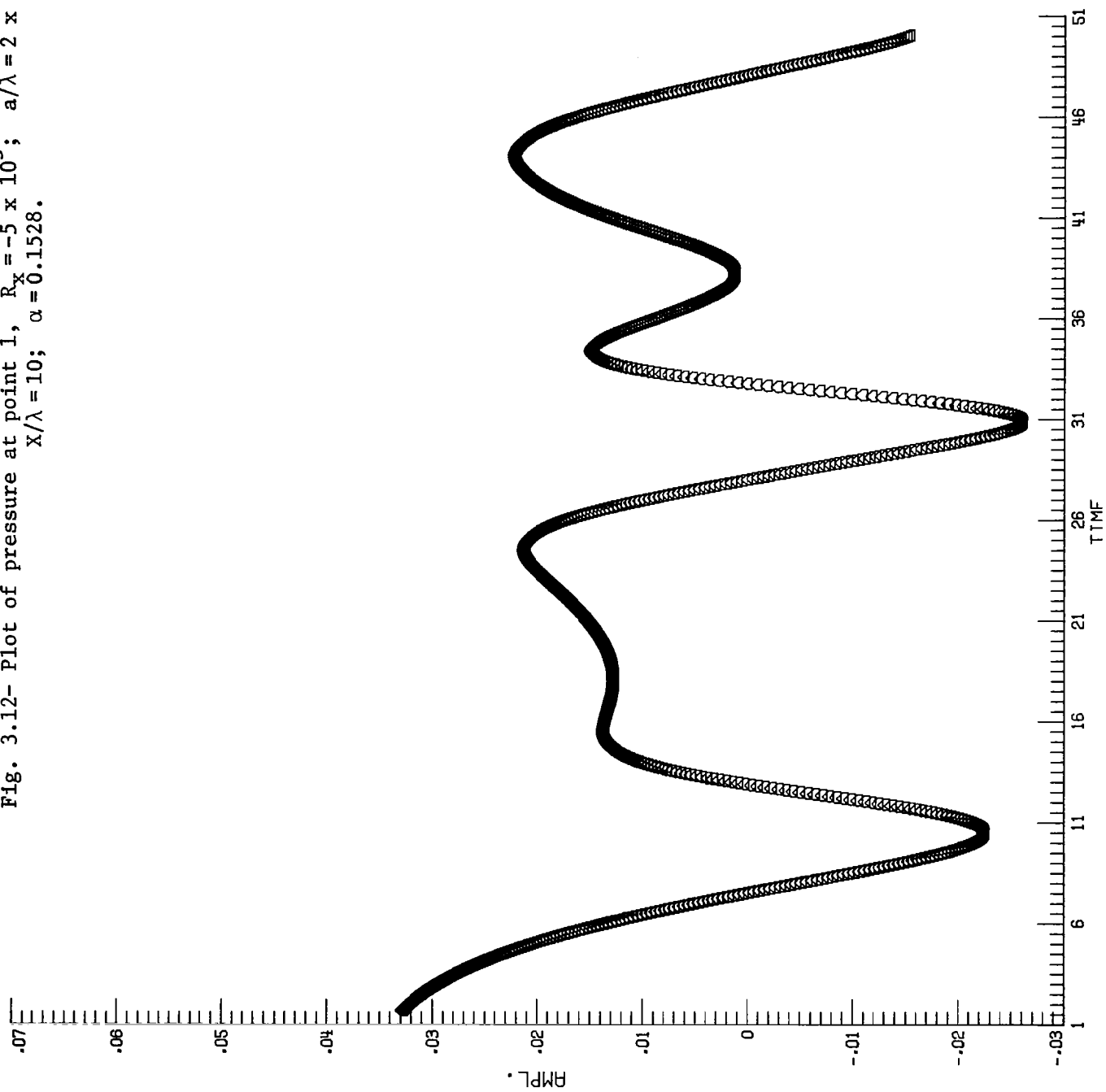


Fig. 3.13- Plot of pressure at point 2 ($\lambda/8$ downstream of point 1)
 $R_x = 5 \times 10^5$; $a/\lambda = 2 \times 10^{-2}$; $X/\lambda = 10$; $\alpha = 0.1528$.

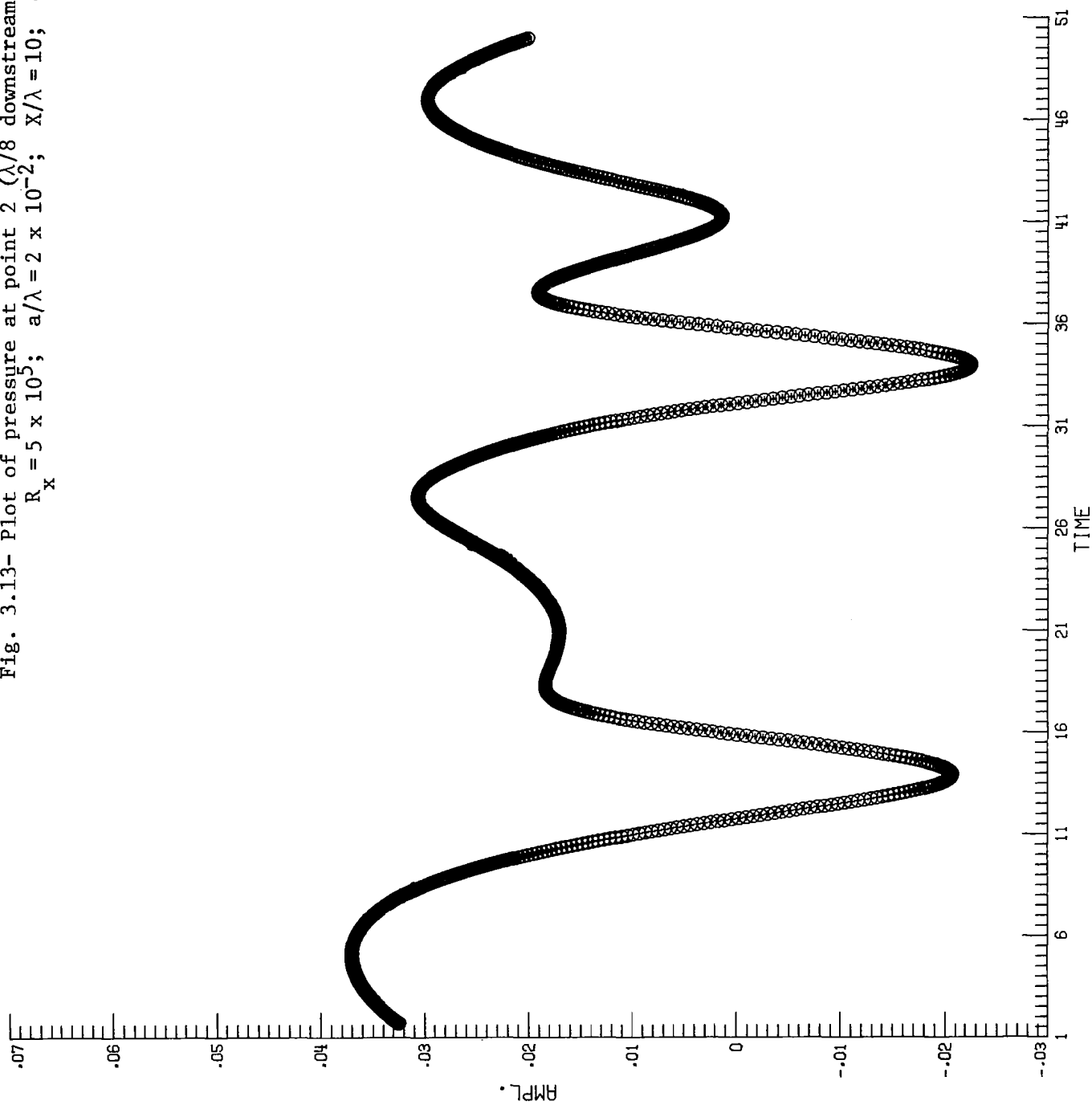


Fig. 4.1- Evolution of Rayleigh solutions.

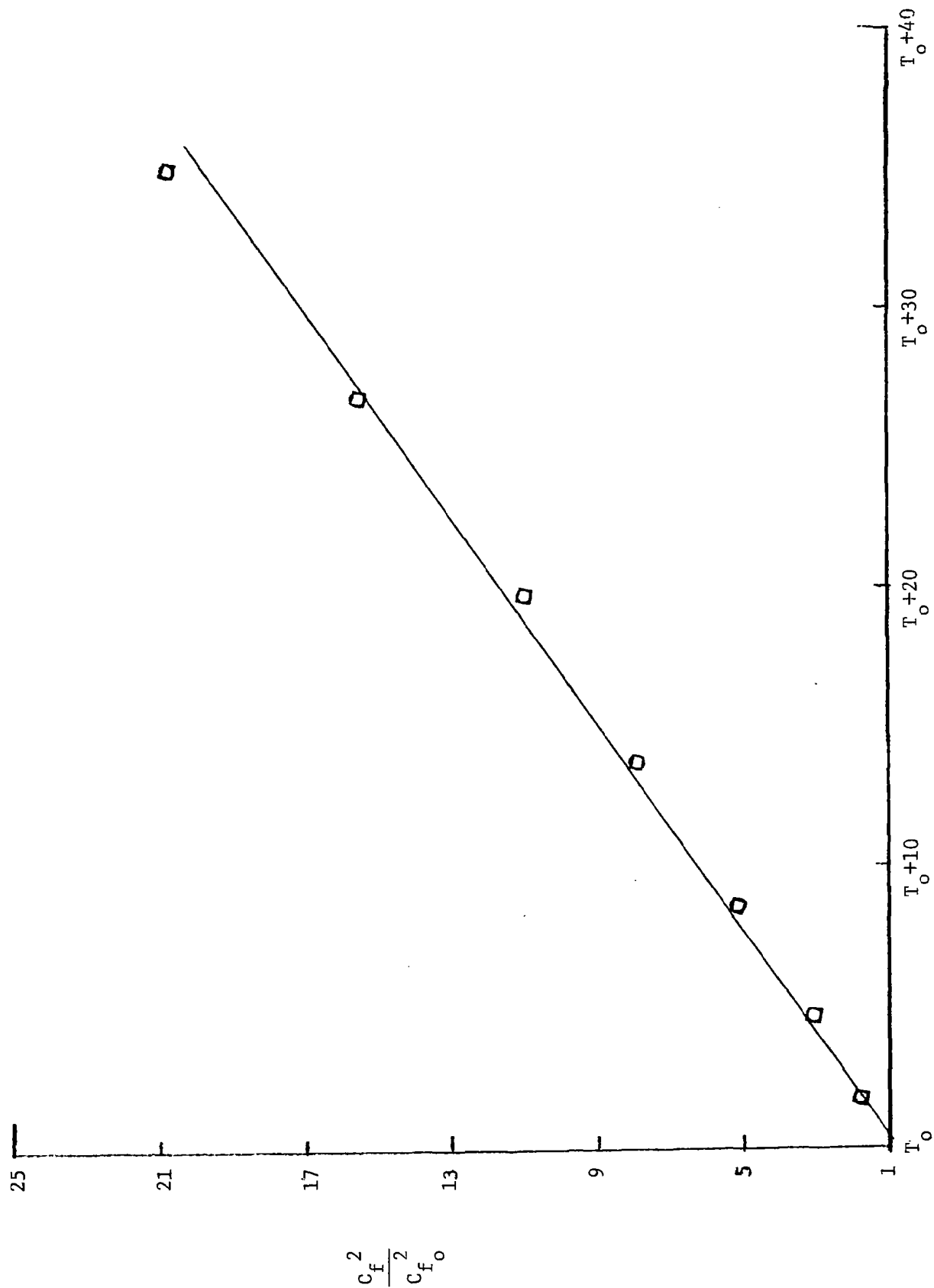


Fig. 4.2- Plot of evolution of solution on a flat plate at Reynolds number $R_{x_0} = 200$ using the periodic Navier Stokes solver.

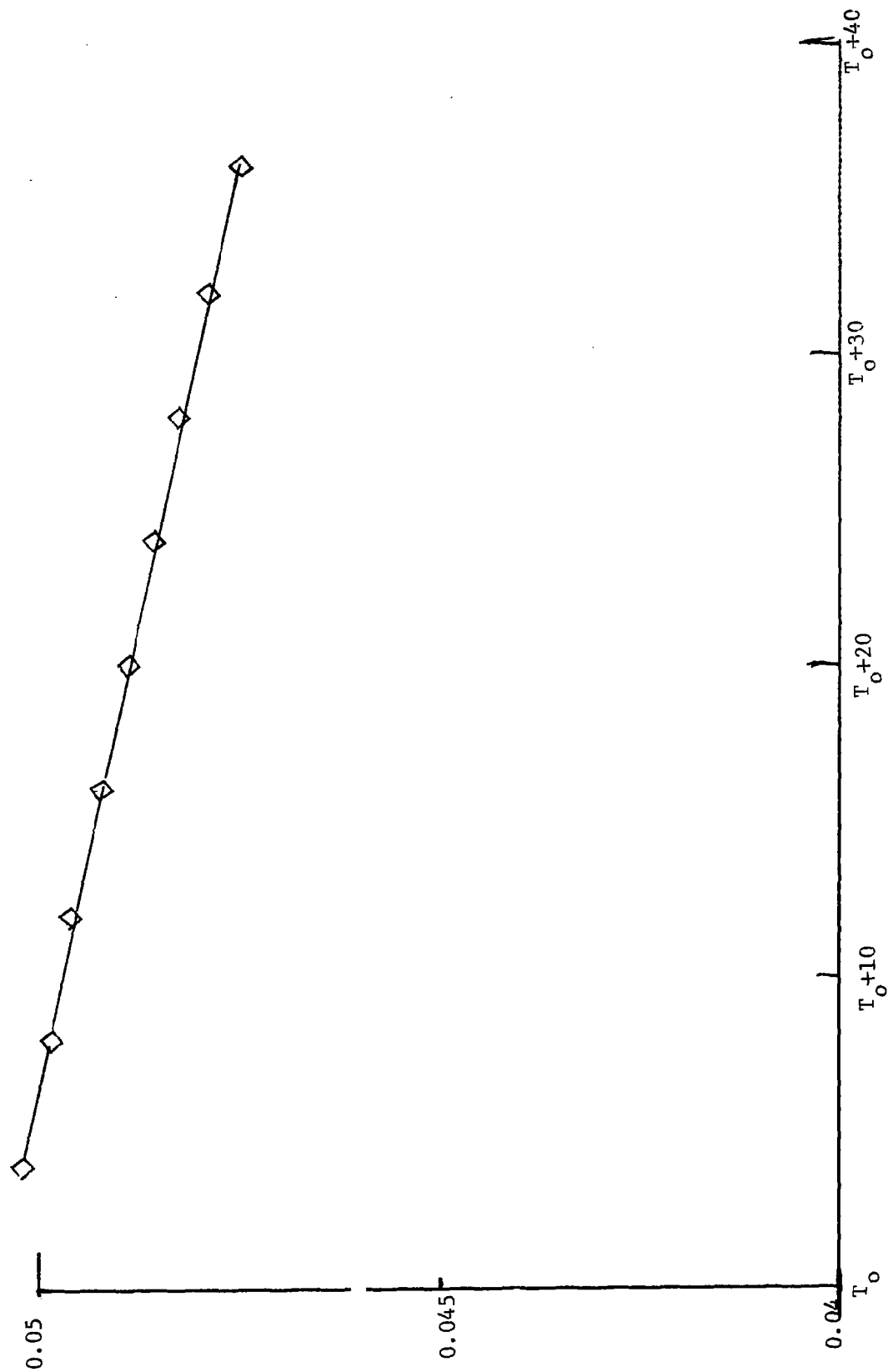


Fig. 4.3- Plot of evolution of solution on a flat plate at Reynolds number $R_{x_0} = 1000$ using the periodic Navier Stokes solver.

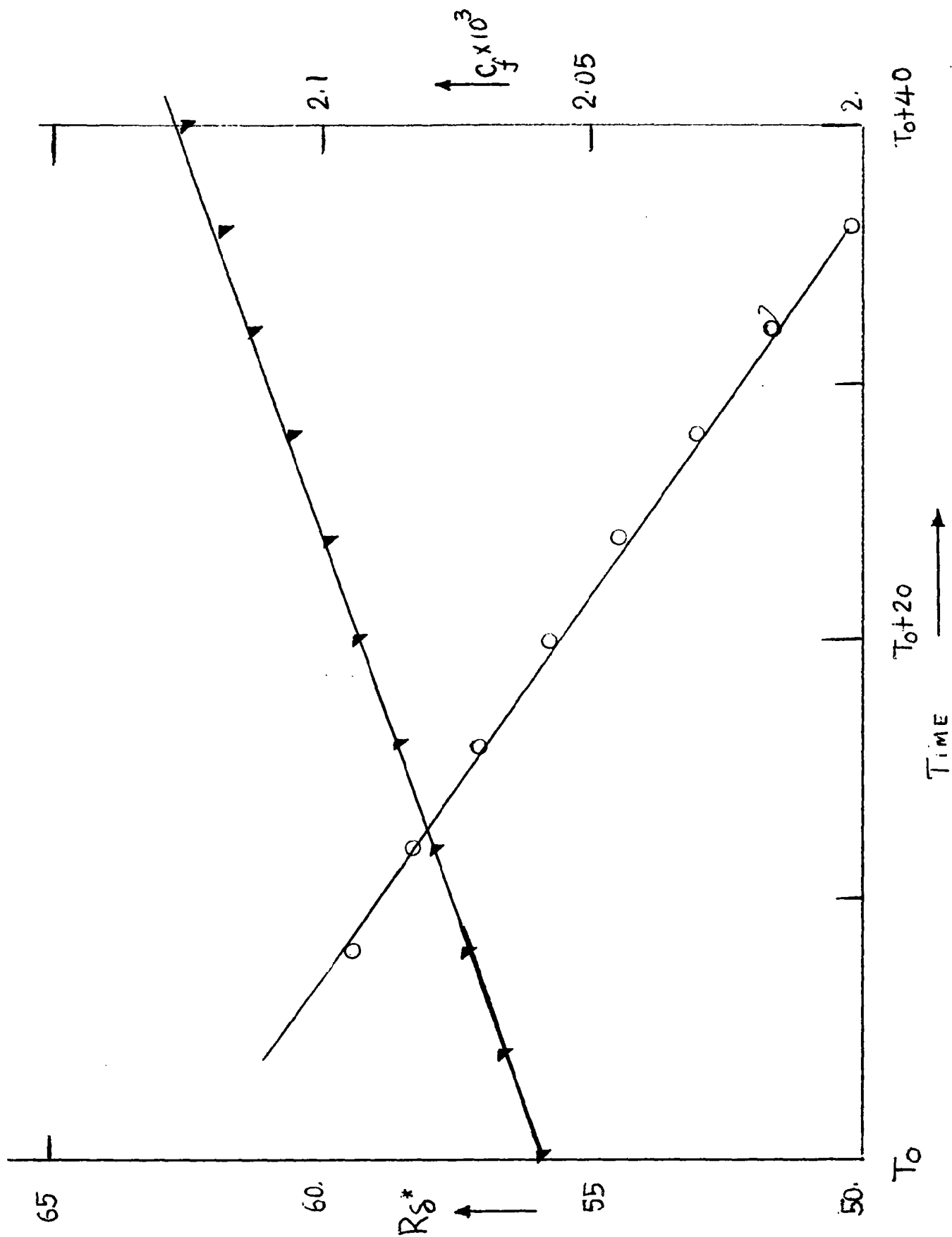


Fig. 5.1- Plot of nonplanar geometries.



Fig. 5.1a- Unsymmetric v-groove .

Fig. 5.1b- Unsymmetric v-groove.

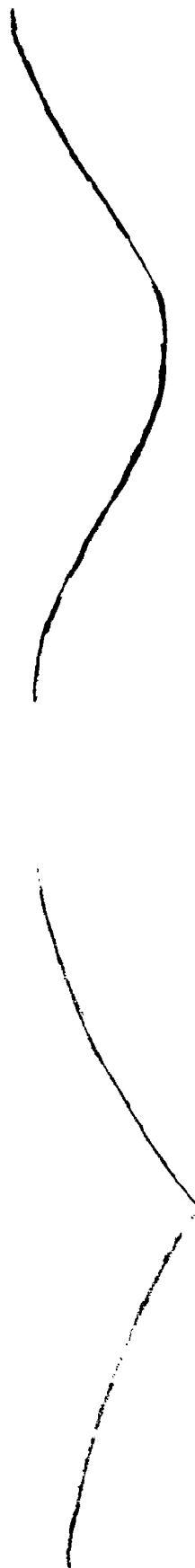


Fig. 5.1c- A symmetric v-groove.

Fig. 5.1d- Sine waveform.

Fig. 5.2- Plot of Drag characteristic of nonplanar waveforms in laminar flow as a function of the Reynolds number of oncoming flow.

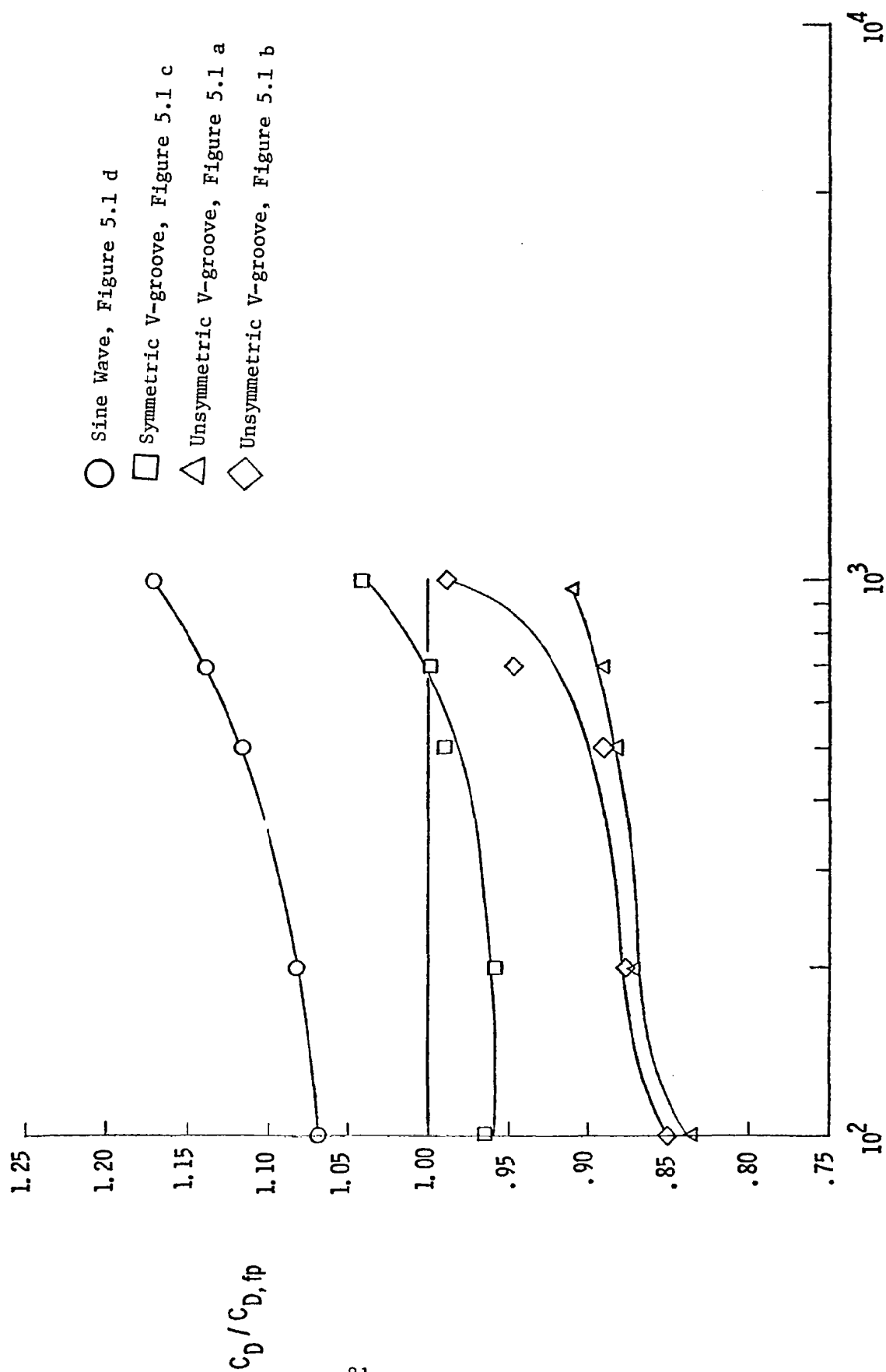


Fig. 6.1- Calibration plot of skin friction distribution over a wave cycle of suction and injection distribution for a flow over a flat plate.

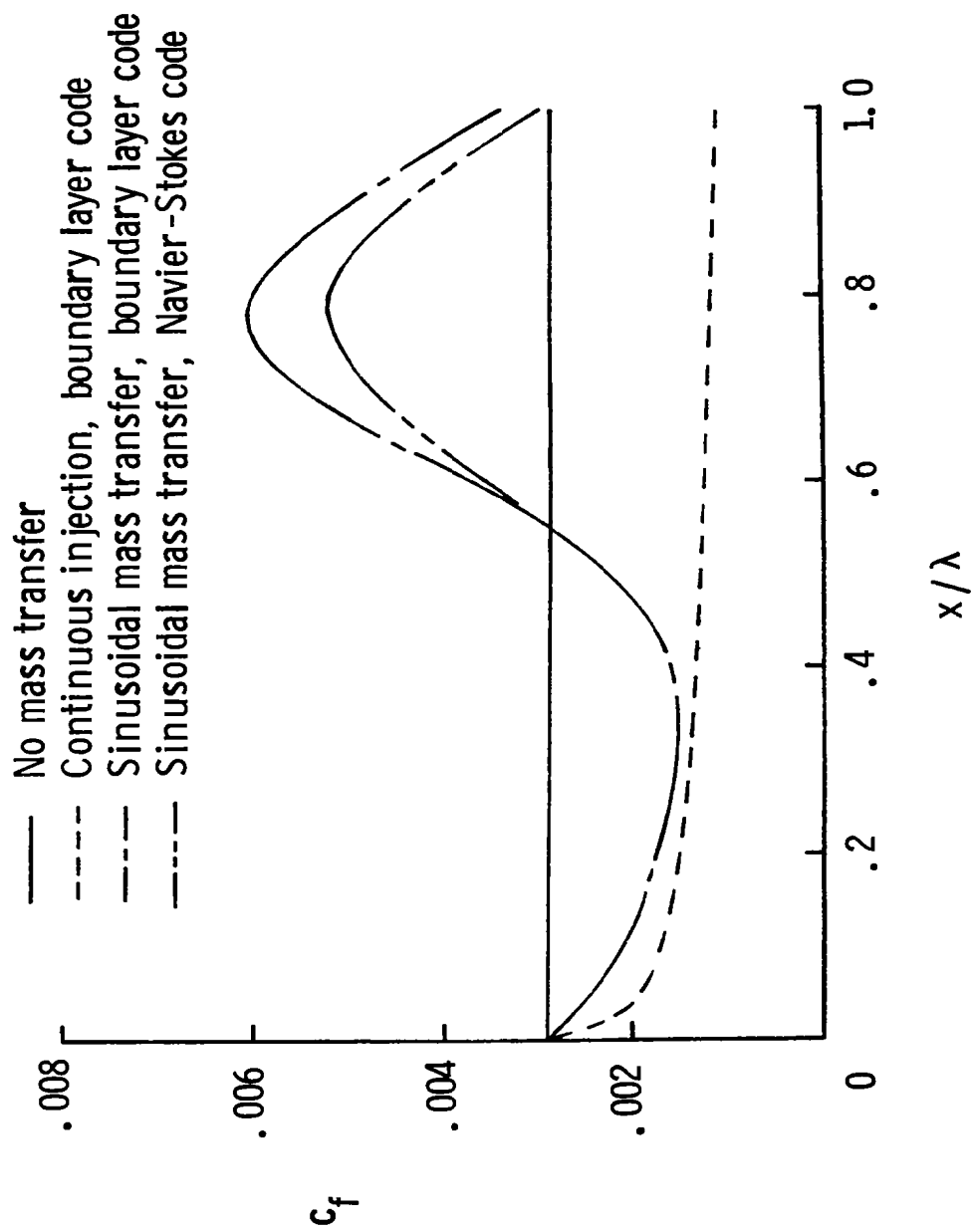
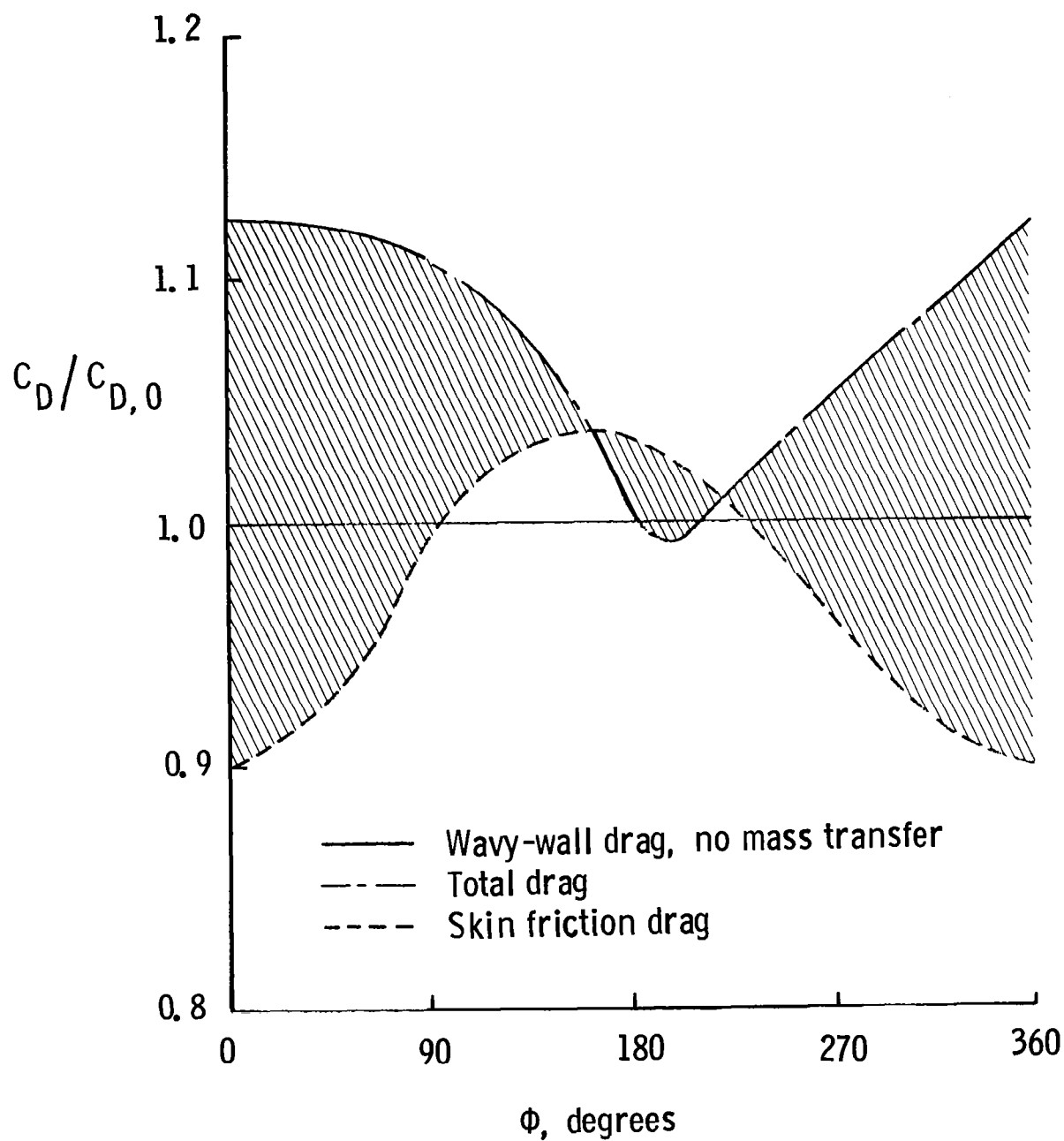


Fig. 6.2- Plot of drag characteristic for a sinusoidal wave as a function of suction phase angle " ϕ " relative to the wave crest.



1. Report No. NASA CR-3669	2. Government Accession No.	3. Recipient's Catalog No.	
4. Title and Subtitle NUMERICAL STUDIES OF LAMINAR AND TURBULENT DRAG REDUCTION - PART II		5. Report Date January 1983	
		6. Performing Organization Code	
7. Author(s) R. Balasubramanian and S. A. Orszag		8. Performing Organization Report No. CHI Report No. 75	
		10. Work Unit No.	
9. Performing Organization Name and Address Cambridge Hydrodynamics, Inc. P. O. Box 249, MIT Station Cambridge, MA 02139		11. Contract or Grant No. NAS1-16722	
		13. Type of Report and Period Covered Contractor Report	
12. Sponsoring Agency Name and Address National Aeronautics and Space Administration Washington, DC 20546		14. Sponsoring Agency Code	
15. Supplementary Notes			
16. Abstract The flow over wave shaped surfaces is studied using a Navier Stokes solver. Detailed comparisons with theoretical results are presented, including the stability of a laminar flow over wavy surfaces. Drag characteristics of nonplanar surfaces is predicted using the Navier-Stokes solver. Also discussed are the secondary instabilities of wall bounded and free shear flows.			
17. Key Words (Suggested by Author(s)) Drag reduction Wavy walls Boundary layers Secondary instability Hydrodynamics stability		18. Distribution Statement Unclassified - Unlimited Subject Category 34	
19. Security Classif. (of this report) Unclassified	20. Security Classif. (of this page) Unclassified	21. No. of Pages 90	22. Price A05